



A double-yield-surface plasticity theory for transversely isotropic rocks

Yang Zhao¹ · Ronaldo I. Borja²

Received: 17 January 2022 / Accepted: 17 May 2022 / Published online: 24 June 2022
© The Author(s), under exclusive licence to Springer-Verlag GmbH Germany, part of Springer Nature 2022

Abstract

We present a double-yield-surface plasticity theory for transversely isotropic rocks that distinguishes between plastic deformation through the solid matrix and localized plasticity along the weak bedding planes. A recently developed anisotropic modified Cam-Clay model is adopted to model the plastic response of the solid matrix, while the Mohr–Coulomb friction law is used to represent the sliding mechanism along the weak bedding planes. For its numerical implementation, we derive an implicit return mapping algorithm for both the semi-plastic and fully plastic loading processes, as well as the corresponding algorithmic tangent operator for finite element problems. We validate the model with triaxial compression test data for three different transversely isotropic rocks and reproduce the undulatory variation of rock strength with bedding plane orientation. We also implement the proposed model in a finite element setting and investigate the deformation of rock surrounding a borehole subjected to fluid injection. We compare the results of simulations using the proposed double-yield-surface model with those generated using each single yield criterion to highlight the features of the proposed theory.

Keywords Double yield surfaces · Frictional sliding · Plasticity · Shale · Transversely isotropic rock

1 Introduction

Anisotropy is a ubiquitous property of natural rocks [108]. Typical anisotropic rocks include sedimentary rocks that possess marked depositional layers such as shale, and foliated metamorphic rocks such as slates, gneisses, phyllites, and schists. The most common type of anisotropy is that of transverse isotropy characterized by parallel or nearly parallel sets of depositional layers or foliations forming a simple laminated structure. Such a laminated internal structure plays a critical role in determining the geophysical [27, 35, 110], hydrologic [44, 45, 103, 104, 106, 107], and mechanical [25, 50, 68, 69, 81, 85, 100] properties of transversely isotropic rocks.

In recent years, numerous investigators have conducted laboratory experiments to quantify and analyze the influence of material anisotropy on the mechanical behaviors of transversely isotropic rocks [2, 10, 19, 27, 54, 56, 60, 73, 98]. Unlike isotropic materials, both the stiffness and the strength of transversely isotropic rocks are dependent on the bedding plane orientation θ in the test specimens, varying in a highly nonlinear fashion. In terms of rock stiffness, the apparent Young's modulus of transversely isotropic rocks often varies with bedding plane orientation as a U-shaped curve [93] or an S-shaped curve [1]. When it comes to rock strength, Ramamurthy [70] classified the variation curves into three groups, namely (a) U-type, (b) shoulder type, and (c) undulatory type of variation [83], as demonstrated in Fig. 1. Among them, the undulatory type exhibits the most complicated characteristics that could be regarded either as a U-type or a shoulder type curve with an additional concave portion within the range $45^\circ < \theta < 90^\circ$, which is the range of bedding plane orientations in rock specimens under which condition of failure along the bedding plane is likely to occur [33, 64, 84, 95].

To describe the variation of rock strength with bedding plane orientation, one common approach is to regard transversely isotropic rocks as a continuum and develop the

✉ Ronaldo I. Borja
borja@stanford.edu

¹ State Key Laboratory of Hydroscience and Engineering, Department of Hydraulic Engineering, Tsinghua University, Beijing 100084, China

² Department of Civil and Environmental Engineering, Stanford University, Stanford, CA 94305, USA

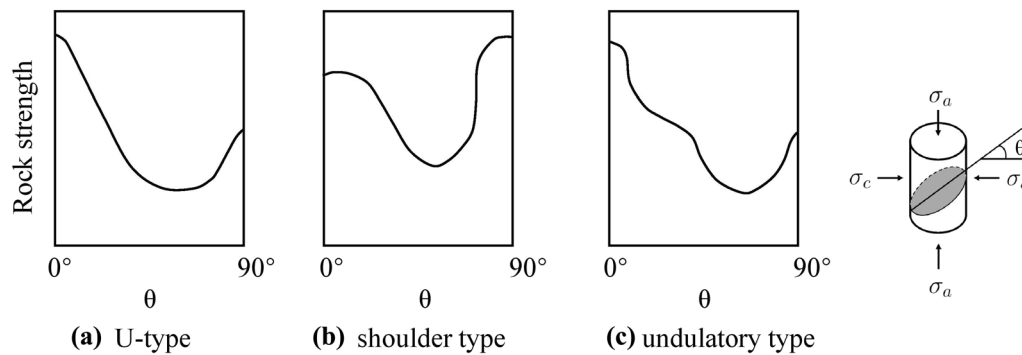


Fig. 1 Variation of rock strength with bedding plane orientation for transversely isotropic rocks. Modified from [70]

corresponding anisotropic elastoplastic constitutive model illustrating their mechanical responses [28, 47, 78, 87, 88, 96]. For anisotropic materials, Gol'denblat and Kopnov [34] proposed a general formulation expressing the yield criterion as a polynomial of stress components for glass-reinforced plastics. Tsai and Wu [86] proposed a yield criterion for filamentary composites as a polynomial that only contains the linear and quadratic terms of stress components.

Alternatively, instead of developing a general expression of the yield criterion for anisotropic materials, a vast majority of the models in the literature extend existing isotropic yield criteria to account for material anisotropy. Hill [40] extended the von Mises yield criterion for metals using six material parameters that scale the second-order stress terms in the yield criterion. Wang et al. [92] extended Hill's criterion by considering the impact of the hydrostatic stress on the yield function, which resulted in an anisotropic version of Drucker–Prager model for transversely isotropic rocks. Boehler and Sawczuk [11] introduced a general method that takes advantage of isotropic plasticity models by substituting a fictitious stress state projected with a rank-four tensor into the yield criterion. Based on this concept, Bennett et al. [9] developed a generalized capped Drucker–Prager model for anisotropic geomaterials with finite deformation. Nova [65] extended the Cam-Clay model for transversely isotropic rocks. Crook et al. [24] extended the modified Cam-clay model using a projection tensor similar to that adopted by Hashagen and de Borst [38]. Semnani et al. [74] and Zhao et al. [108] also enhanced the modified Cam-Clay model with a projection tensor that only has three parameters for transversely isotropic rocks. Borja et al. [17] further enriched this model to consider material heterogeneity and viscoplasticity for shale rocks. Bryant and Sun [18] also refined this model with micromorphic regularization to accommodate size-dependent anisotropy of geomaterials.

Another approach to modeling the behavior of transversely isotropic rocks is to represent the laminated

structure or the matrix-foliation system of the rock explicitly. Representative works include the microplane model [6–8] and the multi-laminate model [66, 111], both of which are based on the concept of angular discretization of space in which the overall material behavior is quantified as the aggregated response on several so-called integration planes where plasticity models are applied. By assigning different plastic parameters to the integration planes according to their spatial angle, this class of models can be used for materials with inherent anisotropy [26, 51, 52]. Crystal plasticity [4, 13, 15, 16, 39, 48, 49, 63, 71] is another common technique to handle materials with inherent microstructures, which adopts multiplane slip systems determined by the crystalline microstructures to describe the plastic responses of single crystals. Semnani and White [72] introduced an inelastic homogenization framework for layered materials. They assumed a laminated microstructure with weak planes where the layers and the interfaces are modeled with various isotropic plasticity models. Through homogenization over such a microstructure, the macroscopic anisotropic responses of transversely isotropic rocks can then be calculated. Choo et al. [23] extended this framework to consider time-dependent responses in the constituent layers and proposed an anisotropic viscoplastic model for shale.

In addition to micromechanical modeling and computational homogenization, the foliations can also be modeled explicitly at the macroscopic level. Tang et al. [82] conducted finite element simulations of uniaxial compression tests on stratified geomaterials in which the foliations were explicitly modeled as bands with a finite width in the simulated specimen with weaker materials. Their simulation can capture different failure modes either through the rock matrix or along the weak planes for specimens with different bedding plane orientation. Various authors have also attempted to explicitly model the matrix-foliation system with discrete element method [32, 55, 61, 67, 75, 94, 99], where the foliation is idealized

as bonds between discrete solid particles at the weak planes governed by discrete constitutive laws that allows for shear or tensile failure, with which macroscopic failure of the specimens along the weak planes can be captured.

Focusing on the strength instead of the constitutive responses, various investigators have also proposed discontinuous failure criteria for transversely isotropic rocks that can account for different failure modes. Pioneering works in this category include the single plane of weakness theory of Jaeger [46], which generalized the Coulomb–Navier criterion for laminated rocks by considering two failure modes, namely failure along the weak planes or through the rock matrix. Based on this idea, Walsh and Brace [89] proposed a failure criterion where the failure of the schistosity planes is governed by a modified Griffith theory. Hoek [41] extended Jaeger’s theory through the application of the Hoek–Brown failure criterion [42] to both the weak planes and the rock matrix. Tien and Kuo [83] extended Jaeger’s theory and proposed a more elaborate criterion for failure through the solid matrix, which adopted the Hoek–Brown failure criterion to distinguish rock strength at $\theta = 0^\circ$ and $\theta = 90^\circ$. A maximum axial strain criterion was then introduced to calibrate the strength of specimens with inclined bedding planes. Jaeger’s theory has also been extended to model rocks with multiple groups of weak planes or joints (see [37, 62, 90]).

Each of the three types of models for the description of the strength of transversely isotropic rocks has its own pros and cons. With the first two types of models, one can reproduce the stress–strain curve of transversely isotropic rocks measured in laboratory tests and capture rock strength naturally [74, 108]. However, for continuum models, the rock is treated as an anisotropic continuum, and the plastic sliding failure mode along the weak planes is seldom considered, making them incapable of reproducing the undulatory type strength variation curve with bedding planes. For models that consider the weak planes explicitly, in theory, they can capture all three types of strength variation curves, but it comes with the disadvantage that many more microscale parameters are needed to calibrate them, accompanied with significant computational costs. For the discontinuous failure criteria, different failure modes are considered and the plastic sliding failure mode along the weak planes is properly captured, and thus the additional concave portion in the undulatory type strength variation curve governed by failure along the weak planes can be modeled. However, the disadvantage of this method is that the failure criterion for the rock matrix has been over-simplified, and it is hard to capture the nonlinearity in the strength variation curve governed by this failure mode. For example, in Jaeger’s theory where the

isotropic Coulomb–Navier criterion is adopted for the rock matrix, rock strength is a constant when the failure mode is through the matrix, which is insufficient to reflect experimental observations demonstrated in Fig. 1. Efforts such as the work of Tien and Kuo [83] tried to make up for this disadvantage by using a more complicated criterion for the rock matrix. Such an enhancement, however, is highly empirical and lacks mathematical foundations.

In this paper, we introduce a double-yield-surface plasticity model for transversely isotropic rocks that combines the advantages of the continuum constitutive model formulation and the discontinuous failure criteria. In the proposed model, we make a clear distinction between bulk plasticity in the rock matrix and sliding mechanism along the weak bedding planes. A recently developed anisotropic modified Cam–Clay model is adopted to model the plastic response of the rock matrix, while the Mohr–Coulomb friction law is used to represent sliding deformation along the weak bedding planes. For the numerical implementation of the proposed model, we derive an implicit return mapping algorithm for different loading processes along with the corresponding algorithmic tangent operator for the solution of finite element problems. We then validate the model by reproducing the undulatory variation of rock strength with bedding plane orientation observed in triaxial compression tests for three different transversely isotropic rocks. Lastly, we implement the model in a finite element framework and conduct boundary value problem simulations to investigate the deformation of surrounding rocks around a borehole subjected to fluid injection.

As for notations and symbols, we use boldfaced characters (e.g., \mathbf{a}) to represent vectors and rank-two tensors, and blackboard bold letters (e.g., \mathbb{I}) to represent rank-four tensors. $\mathbf{1}$ and $\mathbb{1}$ stand for rank-two and rank-four symmetric identity tensors, respectively, and $\mathbb{0}$ is the rank-four zero tensor. Dot product and double dot product are defined with symbols \cdot and $:$, respectively. Tensorial operators \otimes , \oplus and \ominus are defined such that $(\bullet \otimes \circ)_{ijkl} = (\bullet)_{ij}(\circ)_{kl}$, $(\bullet \oplus \circ)_{ijkl} = (\bullet)_{ji}(\circ)_{ik}$, and $(\bullet \ominus \circ)_{ijkl} = (\bullet)_{il}(\circ)_{jk}$.

2 Theoretical formulation

In this section, we introduce the theoretical formulation of the proposed double-yield-surface plasticity model for transversely isotropic rocks. We first introduce the underlying assumptions and the constitutive laws of the proposed model. Next, we present a formulation for double-yield-surface plasticity model, adapted from [12, 43], with explicit definitions of different loading and unloading processes.

2.1 Double-yield-surface formulation

In this model, we assume that a rock can be regarded as a homogenized elastoplastic transversely isotropic continuum. The laminated structure would result in the anisotropic continuous response of the rock matrix, and besides that, the bedding direction of the laminated structure would serve as a weak direction along which plastic sliding could occur. Based on this assumption, the plastic deformation in transversely isotropic rocks can be decomposed into two mechanisms: yielding in the rock matrix and/or yielding along the weak bedding planes. The total strain can thus be expressed as

$$\epsilon = \epsilon^e + \epsilon_m^p + \epsilon_w^p. \tag{1}$$

In this expression, the superscripts *e* and *p* refer to the elastic and plastic parts of the strain tensor, respectively; the subscripts *m* and *w* indicate plastic strain in the rock matrix and along the weak planes, respectively.

To reflect the influence of the laminated structure on the mechanical response of transversely isotropic rocks, we first introduce a rank-two microstructure tensor *m* defined as

$$m = n \otimes n, \tag{2}$$

where *n* stands for the unit normal vector to the bedding planes.

Assuming a linearly elastic material response,

$$\sigma = \mathbb{C}^e : \epsilon^e, \tag{3}$$

where σ is the Cauchy stress tensor and \mathbb{C}^e is the elastic tangent operator. For transversely isotropic rocks, the expression for \mathbb{C}^e is given by [79]

$$\begin{aligned} \mathbb{C}^e = & \lambda \mathbf{1} \otimes \mathbf{1} + 2\mu_T \mathbb{I} + a(\mathbf{1} \otimes m + m \otimes \mathbf{1}) + bm \otimes m \\ & + (\mu_L - \mu_T)(\mathbf{1} \oplus m + m \oplus \mathbf{1} + \mathbf{1} \ominus m + m \ominus \mathbf{1}), \end{aligned} \tag{4}$$

where $\lambda, a, b, \mu_L, \mu_T$ are five material constants.

As for the plastic response, we use two different yield criteria to model ductile deformation mechanisms in the rock matrix and sliding along the weak planes. For the first part, we adopt an anisotropic modified Cam-Clay model introduced by Semnani et al. [74] and Zhao et al. [105, 108] to represent the anisotropic response of the rock matrix. To this end, we introduce a fictitious stress state σ^* as

$$\sigma^* = \mathbb{P} : \sigma, \tag{5}$$

where \mathbb{P} is a rank-four projection tensor defined as

$$\begin{aligned} \mathbb{P} = & c_1 \mathbb{I} + \frac{c_2}{2} (m \oplus m + m \ominus m) \\ & + \frac{c_3}{4} (\mathbf{1} \oplus m + m \oplus \mathbf{1} + \mathbf{1} \ominus m + m \ominus \mathbf{1}), \end{aligned} \tag{6}$$

in which c_1, c_2, c_3 are parameters that control the degree of anisotropy of the yield surface. The projection tensor \mathbb{P} contains the anisotropy information through the microstructure tensor *m*. Inserting σ^* into the isotropic modified Cam-Clay yield surface yields the anisotropic yield function for the rock matrix as

$$f_m(\sigma^*, p_c) = \frac{q^{*2}}{M^2} + p^*(p^* - p_c) \leq 0, \tag{7}$$

where $p^* = \text{tr}(\sigma^*)$, $q^* = \sqrt{3/2} \|s^*\|$, $s^* = \sigma^* - p^*\mathbf{1}$, and $p_c < 0$ is the preconsolidation stress. In terms of the Cauchy stress tensor σ , we have

$$f_m(\sigma, p_c) = \frac{\sigma : \mathbb{A}^* : \sigma}{2M^2} + (a^* : \sigma)(a^* : \sigma - p_c) \leq 0, \tag{8}$$

where

$$a^* = \frac{1}{3} \mathbb{P} : \mathbf{1}, \quad \mathbb{A}^* = 3\mathbb{P} : \left(\mathbb{I} - \frac{1}{3} \mathbf{1} \otimes \mathbf{1} \right) : \mathbb{P}. \tag{9}$$

Assuming an associative flow rule, we can derive the rate of plastic deformation in the rock matrix as

$$\dot{\epsilon}_m^p = \dot{\lambda}_m \frac{\partial f_m}{\partial \sigma} = \dot{\lambda}_m \frac{\partial f_m}{\partial \sigma^*} : \frac{\partial \sigma^*}{\partial \sigma} = \dot{\lambda}_m \mathbb{P} : \frac{\partial f_m}{\partial \sigma^*}, \tag{10}$$

where $\dot{\lambda}_m \geq 0$ is a plastic multiplier for the rock matrix. As for the hardening law, we correlate the preconsolidation stress p_c to the volumetric part of the plastic strain ϵ_v^p as

$$p_c = p_{c0} \exp\left(-\frac{\epsilon_v^p}{\lambda^p}\right), \tag{11}$$

where λ^p is a plastic compressibility index and $\epsilon_v^p = \mathbf{1} : \epsilon_m^p$. Plastic dilation is characterized by $\epsilon_v^p > 0$ while plastic compression is defined by $\epsilon_v^p < 0$.

For sliding mechanism along the weak bedding planes, we adopt the Mohr–Coulomb failure criterion

$$f_w(\tau, \sigma_n) = |\tau| - (c_w - \sigma_n \tan \phi_w) \leq 0, \tag{12}$$

where c_w and ϕ_w are the cohesion and friction angle, and τ and σ_n are the shear and normal stresses on the weak planes, which can be calculated as

$$\sigma_n = n \cdot \sigma \cdot n = \sigma : m, \quad |\tau| = \sqrt{|\sigma \cdot n|^2 - \sigma_n^2}. \tag{13}$$

To prescribe the plastic flow direction, we define the plastic potential function as

$$g_w(\tau, \sigma_n) = |\tau| + \sigma_n \tan \psi_w, \tag{14}$$

where $\psi_w \leq \phi_w$ is the dilatancy angle on the weak planes. The rate of plastic deformation can then be expressed as

$$\dot{\epsilon}_w^p = \dot{\lambda}_w \frac{\partial g_w}{\partial \sigma} = \dot{\lambda}_w \frac{\partial g_w}{\partial \tau} \frac{\partial \tau}{\partial \sigma} + \dot{\lambda}_w \frac{\partial g_w}{\partial \sigma_n} \frac{\partial \sigma_n}{\partial \sigma}, \quad (15)$$

where $\dot{\lambda}_w \geq 0$ is a plastic multiplier for sliding along the weak planes [14].

Figure 2 depicts the yield surfaces under a biaxial compression stress state. The rotated ellipse is the anisotropic modified Cam-Clay yield surface f_m for the solid matrix, while the two rays are the projections of the yield surface f_w for the weak planes. The shaded area represents the elastic region, which is now bounded by the two yield surfaces. For a stress state within the elastic region, both yield functions f_m and f_w are less than zero.

2.2 Definitions of various processes

To illustrate the plastic deformation of transversely isotropic rocks modeled with two distinct yield surfaces f_m and f_w , we first define all possible cases of loading and unloading. Let $\delta\sigma$ be the variation of stress state, i.e., the stress probe. Various processes can be defined as follows:

(a) Elastic process:

$$f_m < 0 \quad \text{or} \quad \left(f_m = 0 \quad \text{and} \quad \frac{\partial f_m}{\partial \sigma} : \delta\sigma < 0 \right), \quad (16a)$$

$$\text{and} \quad f_w < 0 \quad \text{or} \quad \left(f_w = 0 \quad \text{and} \quad \frac{\partial f_w}{\partial \sigma} : \delta\sigma < 0 \right). \quad (16b)$$

The two equations in (16) refer to the process in which the stress state is either inside the yield surface or on the yield surface but unloading.

(b) Semi-plastic loading process on f_m :

$$f_m = 0 \quad \text{and} \quad \frac{\partial f_m}{\partial \sigma} : \delta\sigma > 0, \quad (17a)$$

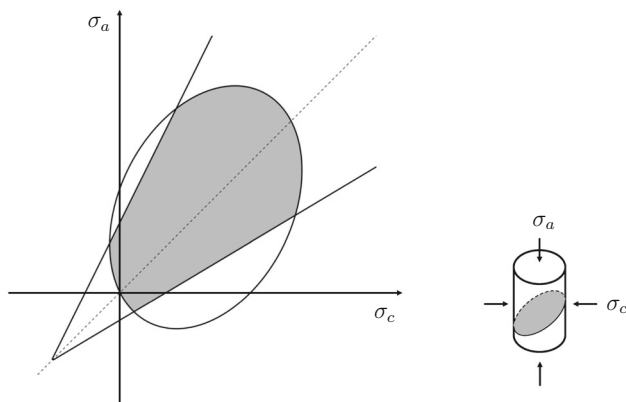


Fig. 2 Sketch of the yield surfaces in the proposed plasticity model for transversely isotropic rocks given a biaxial compression stress state shown in the right figure. The shaded area represents the elastic regime of the proposed plasticity model

$$\text{and} \quad f_w < 0 \quad \text{or} \quad \left(f_w = 0 \quad \text{and} \quad \frac{\partial f_w}{\partial \sigma} : \delta\sigma \leq 0 \right). \quad (17b)$$

For this process, the material yields according to the yield criterion f_m alone.

(c) Semi-plastic loading process on f_w :

$$f_m < 0 \quad \text{or} \quad \left(f_m = 0 \quad \text{and} \quad \frac{\partial f_m}{\partial \sigma} : \delta\sigma \leq 0 \right), \quad (18a)$$

$$\text{and} \quad f_w = 0 \quad \text{and} \quad \frac{\partial f_w}{\partial \sigma} : \delta\sigma > 0. \quad (18b)$$

For this process, the material yields according to the yield criterion f_w alone.

(d) Fully plastic loading process:

$$f_m = 0 \quad \text{and} \quad \frac{\partial f_m}{\partial \sigma} : \delta\sigma > 0, \quad (19a)$$

$$\text{and} \quad f_w = 0 \quad \text{and} \quad \frac{\partial f_w}{\partial \sigma} : \delta\sigma > 0. \quad (19b)$$

For this process, the material yields according to the combined yield criteria f_m and f_w .

(e) Semi-neutral process on f_m :

$$f_m = 0 \quad \text{and} \quad \frac{\partial f_m}{\partial \sigma} : \delta\sigma = 0, \quad (20a)$$

$$\text{and} \quad f_w < 0 \quad \text{or} \quad \left(f_w = 0 \quad \text{and} \quad \frac{\partial f_w}{\partial \sigma} : \delta\sigma < 0 \right). \quad (20b)$$

For this process, the stress state moves tangentially to the yield surface f_m .

(f) Semi-neutral process on f_w :

$$f_m < 0 \quad \text{or} \quad \left(f_m = 0 \quad \text{and} \quad \frac{\partial f_m}{\partial \sigma} : \delta\sigma < 0 \right), \quad (21a)$$

$$\text{and} \quad f_w = 0 \quad \text{and} \quad \frac{\partial f_w}{\partial \sigma} : \delta\sigma = 0. \quad (21b)$$

For this process, the stress state moves tangentially to the yield surface f_w .

(g) Fully neutral process:

$$f_m = 0 \quad \text{and} \quad \frac{\partial f_m}{\partial \sigma} : \delta\sigma = 0, \quad (22a)$$

$$\text{and} \quad f_w = 0 \quad \text{and} \quad \frac{\partial f_w}{\partial \sigma} : \delta\sigma = 0. \quad (22b)$$

For this process, the stress state moves tangentially to both yield surfaces.

2.3 Continuum formulation

In what follows, we consider the continuum formulations for all possible loading/unloading scenarios.

(a) *Fully plastic loading process:*

The consistency conditions for the two yield surfaces are given by

$$\dot{f}_m = \frac{\partial f_m}{\partial \boldsymbol{\sigma}} : \dot{\boldsymbol{\sigma}} + \frac{\partial f_m}{\partial p_c} \dot{p}_c = 0, \quad (23a)$$

$$\dot{f}_w = \frac{\partial f_w}{\partial \boldsymbol{\sigma}} : \dot{\boldsymbol{\sigma}} = 0. \quad (23b)$$

Combining Eqs. (10) and (15), together with the rate form of the elastic constitutive response $\dot{\boldsymbol{\sigma}} = \mathbb{C}^e : (\dot{\boldsymbol{\epsilon}} - \dot{\boldsymbol{\epsilon}}_m^p - \dot{\boldsymbol{\epsilon}}_w^p)$, we can rewrite the consistency conditions as

$$\begin{aligned} \frac{\partial f_m}{\partial \boldsymbol{\sigma}} : \mathbb{C}^e : \left(\dot{\boldsymbol{\epsilon}} - \dot{\lambda}_m \frac{\partial f_m}{\partial \boldsymbol{\sigma}} - \dot{\lambda}_w \frac{\partial g_w}{\partial \boldsymbol{\sigma}} \right) \\ + \frac{\partial f_m}{\partial p_c} \frac{\partial p_c}{\partial \epsilon_v^p} \dot{\lambda}_m \mathbf{1} : \frac{\partial f_m}{\partial \boldsymbol{\sigma}} = 0, \end{aligned} \quad (24a)$$

$$\frac{\partial f_w}{\partial \boldsymbol{\sigma}} : \mathbb{C}^e : \left(\dot{\boldsymbol{\epsilon}} - \dot{\lambda}_m \frac{\partial f_m}{\partial \boldsymbol{\sigma}} - \dot{\lambda}_w \frac{\partial g_w}{\partial \boldsymbol{\sigma}} \right) = 0. \quad (24b)$$

We can then solve for $\dot{\lambda}_m$ and $\dot{\lambda}_w$ using the equations above. By collecting terms and rearranging the expressions, we can reorganize the two equations into matrix form,

$$\begin{bmatrix} \alpha_{11} & \alpha_{12} \\ \alpha_{21} & \alpha_{22} \end{bmatrix} \begin{Bmatrix} \dot{\lambda}_m \\ \dot{\lambda}_w \end{Bmatrix} = \begin{Bmatrix} b_1 \\ b_2 \end{Bmatrix} \quad (25)$$

where

$$\alpha_{11} = \frac{\partial f_m}{\partial \boldsymbol{\sigma}} : \mathbb{C}^e : \frac{\partial f_m}{\partial \boldsymbol{\sigma}} - \frac{\partial f_m}{\partial p_c} \frac{\partial p_c}{\partial \epsilon_v^p} \mathbf{1} : \frac{\partial f_m}{\partial \boldsymbol{\sigma}}, \quad (26a)$$

$$\alpha_{12} = \alpha_{21} = \frac{\partial f_m}{\partial \boldsymbol{\sigma}} : \mathbb{C}^e : \frac{\partial g_w}{\partial \boldsymbol{\sigma}}, \quad (26b)$$

$$\alpha_{22} = \frac{\partial f_w}{\partial \boldsymbol{\sigma}} : \mathbb{C}^e : \frac{\partial g_w}{\partial \boldsymbol{\sigma}}. \quad (26c)$$

and

$$b_1 = \frac{\partial f_m}{\partial \boldsymbol{\sigma}} : \mathbb{C}^e : \dot{\boldsymbol{\epsilon}}, \quad (27a)$$

$$b_2 = \frac{\partial f_w}{\partial \boldsymbol{\sigma}} : \mathbb{C}^e : \dot{\boldsymbol{\epsilon}}. \quad (27b)$$

From Eq. (25), we can see that $\dot{\lambda}_m$ and $\dot{\lambda}_w$ can be solved when the parameter matrix is invertible, and

$$\begin{Bmatrix} \dot{\lambda}_m \\ \dot{\lambda}_w \end{Bmatrix} = \begin{bmatrix} \alpha'_{11} & \alpha'_{12} \\ \alpha'_{21} & \alpha'_{22} \end{bmatrix} \begin{Bmatrix} b_1 \\ b_2 \end{Bmatrix} \quad (28)$$

where

$$\begin{bmatrix} \alpha'_{11} & \alpha'_{12} \\ \alpha'_{21} & \alpha'_{22} \end{bmatrix} = \begin{bmatrix} \alpha_{11} & \alpha_{12} \\ \alpha_{21} & \alpha_{22} \end{bmatrix}^{-1} \quad (29)$$

is the inverse of the parameter matrix.

Inserting Eq. (28) into the rate form of the elastic constitutive response gives

$$\begin{aligned} \dot{\boldsymbol{\sigma}} &= \mathbb{C}^e : (\dot{\boldsymbol{\epsilon}} - \dot{\boldsymbol{\epsilon}}_m^p - \dot{\boldsymbol{\epsilon}}_w^p), \\ &= \left(\mathbb{C}^e - \alpha'_{11} \mathbb{C}^e : \frac{\partial f_m}{\partial \boldsymbol{\sigma}} \otimes \frac{\partial f_m}{\partial \boldsymbol{\sigma}} : \mathbb{C}^e - \alpha'_{12} \mathbb{C}^e : \frac{\partial f_m}{\partial \boldsymbol{\sigma}} \otimes \frac{\partial f_w}{\partial \boldsymbol{\sigma}} : \mathbb{C}^e \right. \\ &\quad \left. - \alpha'_{21} \mathbb{C}^e : \frac{\partial g_w}{\partial \boldsymbol{\sigma}} \otimes \frac{\partial f_m}{\partial \boldsymbol{\sigma}} : \mathbb{C}^e - \alpha'_{22} \mathbb{C}^e : \frac{\partial g_w}{\partial \boldsymbol{\sigma}} \otimes \frac{\partial f_w}{\partial \boldsymbol{\sigma}} : \mathbb{C}^e \right) : \dot{\boldsymbol{\epsilon}} \\ &= \mathbb{C}^{ep} : \dot{\boldsymbol{\epsilon}}, \end{aligned} \quad (30)$$

From the expression above, we see that the elastoplastic tangent operator of the material is given as

$$\begin{aligned} \mathbb{C}^{ep} &= \mathbb{C}^e - \alpha'_{11} \mathbb{C}^e : \frac{\partial f_m}{\partial \boldsymbol{\sigma}} \otimes \frac{\partial f_m}{\partial \boldsymbol{\sigma}} : \mathbb{C}^e - \alpha'_{12} \mathbb{C}^e : \frac{\partial f_m}{\partial \boldsymbol{\sigma}} \otimes \frac{\partial f_w}{\partial \boldsymbol{\sigma}} : \mathbb{C}^e \\ &\quad - \alpha'_{21} \mathbb{C}^e : \frac{\partial g_w}{\partial \boldsymbol{\sigma}} \otimes \frac{\partial f_m}{\partial \boldsymbol{\sigma}} : \mathbb{C}^e - \alpha'_{22} \mathbb{C}^e : \frac{\partial g_w}{\partial \boldsymbol{\sigma}} \otimes \frac{\partial f_w}{\partial \boldsymbol{\sigma}} : \mathbb{C}^e. \end{aligned} \quad (31)$$

(b) *Semi-plastic loading process on f_m :*

For this case, the plastic deformation of the material is governed by the yield surface f_m while the yield surface f_w is inactive. We can write the elastic constitutive response as

$$\dot{\boldsymbol{\sigma}} = \mathbb{C}^e : (\dot{\boldsymbol{\epsilon}} - \dot{\boldsymbol{\epsilon}}_m^p) = \mathbb{C}^{ep} : \dot{\boldsymbol{\epsilon}}, \quad (32)$$

and the simplified consistency condition shown in Eq. (24a) as

$$\frac{\partial f_m}{\partial \boldsymbol{\sigma}} : \mathbb{C}^e : \left(\dot{\boldsymbol{\epsilon}} - \dot{\lambda}_m \frac{\partial f_m}{\partial \boldsymbol{\sigma}} \right) + \frac{\partial f_m}{\partial p_c} \frac{\partial p_c}{\partial \epsilon_v^p} \dot{\lambda}_m \mathbf{1} : \frac{\partial f_m}{\partial \boldsymbol{\sigma}} = 0, \quad (33)$$

from which we can solve for the plastic multiplier $\dot{\lambda}_m$:

$$\alpha_{11} \dot{\lambda}_m = b_1, \quad (34)$$

where

$$\alpha_{11} = \frac{\partial f_m}{\partial \boldsymbol{\sigma}} : \mathbb{C}^e : \frac{\partial f_m}{\partial \boldsymbol{\sigma}} - \frac{\partial f_m}{\partial p_c} \frac{\partial p_c}{\partial \epsilon_v^p} \mathbf{1} : \frac{\partial f_m}{\partial \boldsymbol{\sigma}}, \quad (35)$$

and

$$b_1 = \frac{\partial f_m}{\partial \boldsymbol{\sigma}} : \mathbb{C}^e : \dot{\boldsymbol{\epsilon}}. \quad (36)$$

The elastoplastic tangent operator for this process can be expressed as

$$\mathbb{C}^{ep} = \mathbb{C}^e - \alpha_{11}^{-1} \mathbb{C}^e : \frac{\partial f_m}{\partial \boldsymbol{\sigma}} \otimes \frac{\partial f_m}{\partial \boldsymbol{\sigma}} : \mathbb{C}^e. \quad (37)$$

(c) *Semi-plastic loading process on f_w :*

For this case, the plastic deformation of the material is governed by the yield surface f_w while the yield surface f_m

is inactive. Again, we can write the elastic constitutive response as

$$\dot{\sigma} = \mathbb{C}^e : (\dot{\epsilon} - \dot{\epsilon}_w^p) = \mathbb{C}^{ep} : \dot{\epsilon}, \tag{38}$$

and for this case, the simplified consistency condition shown in Eq. (24b) as

$$\frac{\partial f_w}{\partial \sigma} : \mathbb{C}^e : \left(\dot{\epsilon} - \dot{\lambda}_w \frac{\partial g_w}{\partial \sigma} \right) = 0, \tag{39}$$

from which we can solve for the plastic multiplier $\dot{\lambda}_w$:

$$\alpha_{22} \dot{\lambda}_w = b_2, \tag{40}$$

where

$$\alpha_{22} = \frac{\partial f_w}{\partial \sigma} : \mathbb{C}^e : \frac{\partial g_w}{\partial \sigma}, \tag{41}$$

and

$$b_2 = \frac{\partial f_w}{\partial \sigma} : \mathbb{C}^e : \dot{\epsilon}. \tag{42}$$

The elastoplastic tangent operator for this process can be expressed as

$$\mathbb{C}^{ep} = \mathbb{C}^e - \alpha_{22}^{-1} \mathbb{C}^e : \frac{\partial g_w}{\partial \sigma} \otimes \frac{\partial f_w}{\partial \sigma} : \mathbb{C}^e. \tag{43}$$

The relevant partial derivatives are summarized in Appendix A.

3 Numerical implementation

This section presents the numerical implementation of the double-yield-surface plasticity model at the stress point level, covering both an implicit return mapping algorithm and the derivation of the algorithmic tangent operator.

From loading step n to loading step $n + 1$, the return mapping algorithm iteratively calculates the state variables ϵ_{n+1}^e , $\epsilon_{m,n+1}^p$, $\epsilon_{w,n+1}^p$, σ_{n+1} , and $p_{c,n+1}$ from given incremental strain tensor $\Delta\epsilon$ and starting values of the state variables at loading step n . The iteration is based on a predictor-corrector scheme. First, a trial elastic stress predictor σ_{n+1}^{tr} is calculated as

$$\sigma_{n+1}^{tr} = \sigma_n + \mathbb{C}^e : \Delta\epsilon, \tag{44}$$

which is then used to identify the active constraint(s).

In single yield surface plasticity theory, a trial elastic stress predictor σ_{n+1}^{tr} that lies outside the yield surface automatically implies that the yield surface is active. However, this is not necessarily the case for double-yield-surface plasticity theory. Figure 3 portrays three possible regions outside the two yield surfaces where the elastic stress predictor σ_{n+1}^{tr} could land. When σ_{n+1}^{tr} lands in

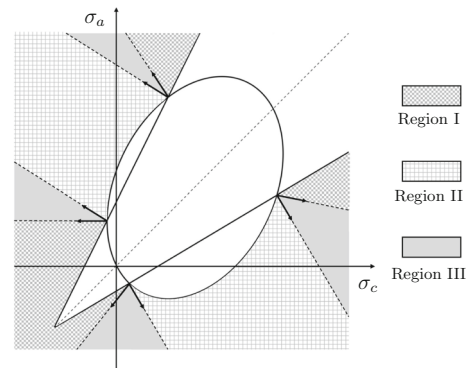


Fig. 3 Possible locations of the trial stress state σ_{n+1}^{tr} outside the two yield surfaces. Arrows represent the normal vectors to the yield surfaces

Region I, the process is semi-plastic on f_m even though $f_w(\sigma_{n+1}^{tr}) > 0$. In Region II, the process is semi-plastic on f_w for the same reason. The process is fully plastic only when σ_{n+1}^{tr} lands in Region III, requiring that the predictor stress be corrected and mapped back to the intersection of the two yield surfaces. In addition, the hardening or softening of f_m can also impact the final process as well as the final position of the stress point σ_{n+1} .

Simo et al. [76] introduced a general return mapping algorithm for multi-surface plasticity model in which the potentially active yield surfaces are first identified based on the value of the trial elastic stress predictor. A first sweep is conducted to calculate the preliminary values of the plastic multipliers for the potentially active constraints. Yield surfaces for which the incremental plastic multipliers are negative are eliminated. The iteration is considered to have converged when all yield criteria are satisfied and all plastic multipliers are nonnegative, i.e., when the discrete Kuhn–Tucker conditions are satisfied on all yield constraints. However, Borja and Wren [13] noted that this algorithm can fail to identify some active constraints, particularly when they are redundant constraints, which led them to develop an ‘ultimate algorithm’ for identifying active constraints in crystals.

We adopt a slightly different approach in the present work. Instead, we first assume that the process is semi-plastic on either f_w or f_m . Then, we assume a fully plastic process if the corrected stress state does not satisfy the yield criterion for the other yield surface. A final correction is made if it was the other yield surface that was active. Figure 4 summarizes the return mapping algorithm adopted in this paper. Details of the formulations are given below.

(a) *Fully plastic loading process:*

For the fully plastic loading process, both yield surfaces f_m and f_w are active and the stress state is mapped back to the intersection of the two yield surfaces. In this case, we

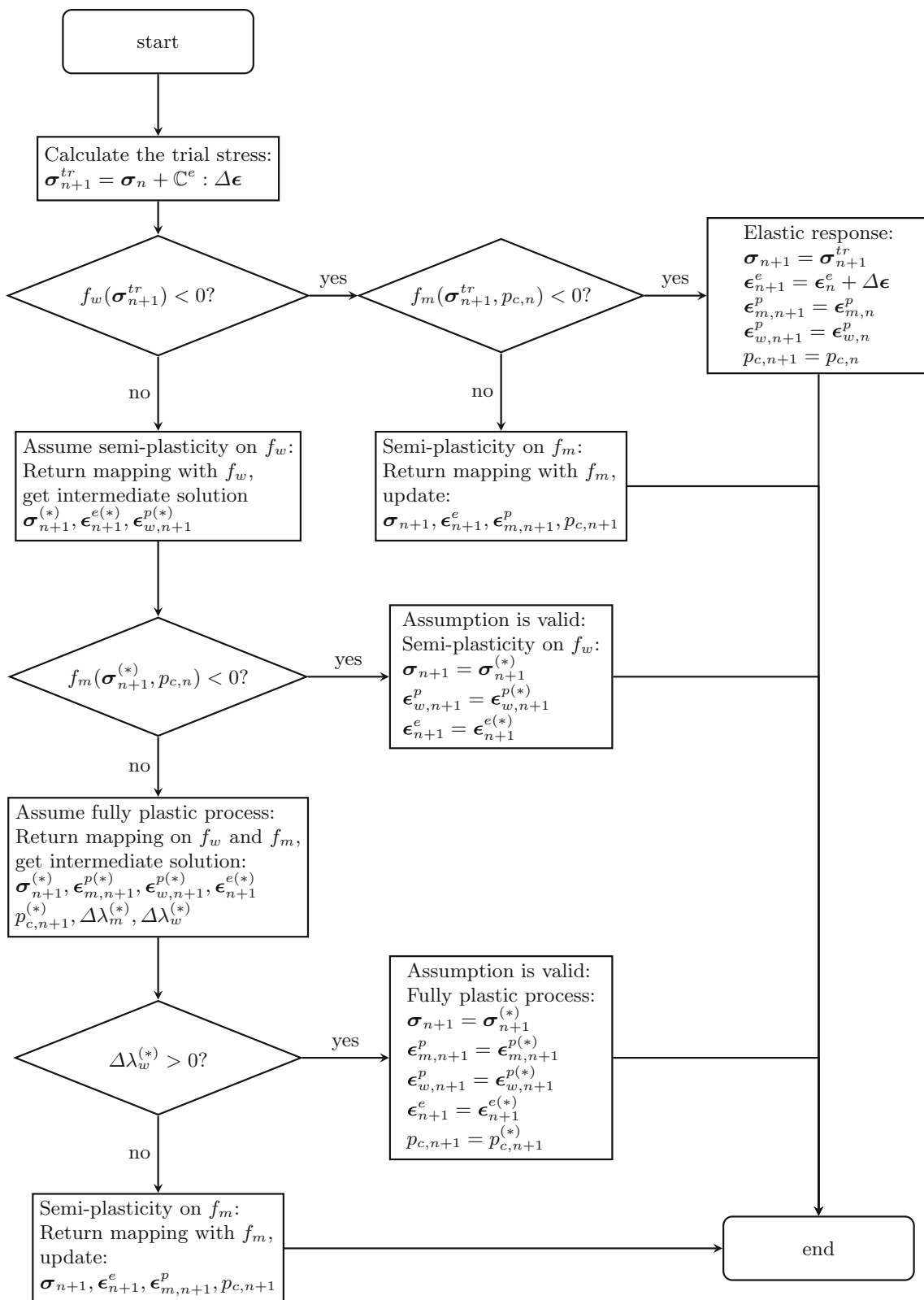


Fig. 4 Return mapping algorithm for the double-yield-surface plasticity model

impose the discrete consistency conditions for both yield surfaces

$$f_m(\boldsymbol{\sigma}_{n+1}, p_{c,n+1}) = 0, \tag{45a}$$

$$f_w(\boldsymbol{\sigma}_{n+1}) = 0, \tag{45b}$$

and the discrete versions of the flow rules

$$\boldsymbol{\epsilon}_{m,n+1}^p - \boldsymbol{\epsilon}_{m,n}^p = \Delta\lambda_m \frac{\partial f_m}{\partial \boldsymbol{\sigma}}, \tag{46a}$$

$$\boldsymbol{\epsilon}_{w,n+1}^p - \boldsymbol{\epsilon}_{w,n}^p = \Delta\lambda_w \frac{\partial g_w}{\partial \boldsymbol{\sigma}}. \tag{46b}$$

The aim is to update the state variables $\boldsymbol{\epsilon}_{m,n+1}^p, \boldsymbol{\epsilon}_{w,n+1}^p$ and the two plastic multipliers $\Delta\lambda_m$ and $\Delta\lambda_w$. To this end, we employ the Newton-Raphson scheme and define the residuals as

$$\mathcal{R}_1 = f_m(\boldsymbol{\sigma}_{n+1}, p_{c,n+1}), \tag{47a}$$

$$\mathcal{R}_2 = -\boldsymbol{\epsilon}_{m,n+1}^p + \boldsymbol{\epsilon}_{m,n}^p + \Delta\lambda_m \frac{\partial f_m}{\partial \boldsymbol{\sigma}}, \tag{47b}$$

$$\mathcal{R}_3 = f_w(\boldsymbol{\sigma}_{n+1}), \tag{47c}$$

$$\mathcal{R}_4 = -\boldsymbol{\epsilon}_{w,n+1}^p + \boldsymbol{\epsilon}_{w,n}^p + \Delta\lambda_w \frac{\partial g_w}{\partial \boldsymbol{\sigma}}, \tag{47d}$$

where \mathcal{R}_1 and \mathcal{R}_3 are scalars, while \mathcal{R}_2 and \mathcal{R}_4 are 6×1 vectors converted from rank-two tensors in Voigt notation. We define the total residual vector \mathcal{R} as

$$\mathcal{R} = [\mathcal{R}_1 \quad \mathcal{R}_2 \quad \mathcal{R}_3 \quad \mathcal{R}_4]^\top \tag{48}$$

and the total unknown vector \mathbf{x} as

$$\mathbf{x} = [\Delta\lambda_m \quad \boldsymbol{\epsilon}_{m,n+1}^p \quad \Delta\lambda_w \quad \boldsymbol{\epsilon}_{w,n+1}^p]^\top. \tag{49}$$

Both \mathcal{R} and \mathbf{x} are of size 14×1 in 3D.

The linearized system takes the form

$$\mathcal{J} \delta \mathbf{x} = -\mathcal{R}, \tag{50}$$

where $\mathcal{J} = \partial \mathcal{R} / \partial \mathbf{x}$ is the Jacobian matrix and $\delta \mathbf{x}$ is the search direction [14]. To be more specific, the equation above can be expanded as

$$\begin{bmatrix} \mathcal{J}_{11} & \mathcal{J}_{12} & \mathcal{J}_{13} & \mathcal{J}_{14} \\ \mathcal{J}_{21} & \mathcal{J}_{22} & \mathcal{J}_{23} & \mathcal{J}_{24} \\ \mathcal{J}_{31} & \mathcal{J}_{32} & \mathcal{J}_{33} & \mathcal{J}_{34} \\ \mathcal{J}_{41} & \mathcal{J}_{42} & \mathcal{J}_{43} & \mathcal{J}_{44} \end{bmatrix} \begin{Bmatrix} \delta \Delta\lambda_m \\ \delta \boldsymbol{\epsilon}_{m,n+1}^p \\ \delta \Delta\lambda_w \\ \delta \boldsymbol{\epsilon}_{w,n+1}^p \end{Bmatrix} = - \begin{Bmatrix} \mathcal{R}_1 \\ \mathcal{R}_2 \\ \mathcal{R}_3 \\ \mathcal{R}_4 \end{Bmatrix}, \tag{51}$$

where the components of \mathcal{J} are derived in Appendix B.

We note that the following state variables vary with the unknown vector \mathbf{x} :

$$\boldsymbol{\epsilon}_{n+1}^e = \boldsymbol{\epsilon}_{n+1} - \boldsymbol{\epsilon}_{m,n+1}^p - \boldsymbol{\epsilon}_{w,n+1}^p, \tag{52a}$$

$$\boldsymbol{\sigma}_{n+1} = \mathbb{C}^e : \boldsymbol{\epsilon}_{n+1}^e, \tag{52b}$$

$$p_{c,n+1} = p_{c0} \exp\left(-\frac{\mathbf{1} : \boldsymbol{\epsilon}_{m,n+1}^p}{\lambda_p}\right). \tag{52c}$$

In evaluating the algorithmic tangent operator \mathbb{C} , we regard $\Delta \boldsymbol{\epsilon}$ and \mathbf{x} as functions of the prescribed total strain $\boldsymbol{\epsilon}_{n+1}$. Thus, we have

$$\mathbb{C} = \mathbb{C}^e : \left(\mathbb{I} - \frac{\partial \boldsymbol{\epsilon}_{m,n+1}^p}{\partial \boldsymbol{\epsilon}_{n+1}} - \frac{\partial \boldsymbol{\epsilon}_{w,n+1}^p}{\partial \boldsymbol{\epsilon}_{n+1}} \right). \tag{53}$$

To derive the expression $\partial \boldsymbol{\epsilon}_{m,n+1}^p / \partial \boldsymbol{\epsilon}_{n+1}$ and $\partial \boldsymbol{\epsilon}_{w,n+1}^p / \partial \boldsymbol{\epsilon}_{n+1}$, we make use of the fact that at the locally converged state,

$$\frac{\partial \mathcal{R}}{\partial \boldsymbol{\epsilon}_{n+1}} = \frac{\partial \mathcal{R}}{\partial \mathbf{x}} \Big|_{\Delta \boldsymbol{\epsilon}} \frac{\partial \mathbf{x}}{\partial \boldsymbol{\epsilon}_{n+1}} + \frac{\partial \mathcal{R}}{\partial \Delta \boldsymbol{\epsilon}} \Big|_{\mathbf{x}} \frac{\partial \Delta \boldsymbol{\epsilon}}{\partial \boldsymbol{\epsilon}_{n+1}} = \mathbf{0}, \tag{54}$$

where

$$\frac{\partial \mathcal{R}}{\partial \mathbf{x}} \Big|_{\Delta \boldsymbol{\epsilon}} = \mathcal{J}, \tag{55a}$$

$$\frac{\partial \Delta \boldsymbol{\epsilon}}{\partial \boldsymbol{\epsilon}_{n+1}} = \mathbb{I}. \tag{55b}$$

Thus, we have

$$\frac{\partial \mathbf{x}}{\partial \boldsymbol{\epsilon}_{n+1}} = \mathcal{J}^{-1} \frac{\partial \mathcal{R}}{\partial \Delta \boldsymbol{\epsilon}} \Big|_{\mathbf{x}}, \tag{56}$$

and the remaining term is derived as

$$\frac{\partial \mathcal{R}}{\partial \Delta \boldsymbol{\epsilon}} \Big|_{\mathbf{x}} = \begin{bmatrix} \frac{\partial f_m}{\partial \boldsymbol{\sigma}} : \mathbb{C}^e \\ \Delta\lambda_m \frac{\partial^2 f_m}{\partial \boldsymbol{\sigma}^2} : \mathbb{C}^e \\ \frac{\partial f_w}{\partial \boldsymbol{\sigma}} : \mathbb{C}^e \\ \Delta\lambda_w \frac{\partial^2 g_w}{\partial \boldsymbol{\sigma}^2} : \mathbb{C}^e \end{bmatrix}_{14 \times 6}, \tag{57}$$

The components are expressed in tensorial form for brevity, but one should note that the rank-two and rank-four tensors in 3D should be converted to 1×6 vectors and 6×6 matrices in Voigt form, respectively.

By combining Eqs. (56) and (57), we can evaluate $\partial \mathbf{x} / \partial \boldsymbol{\epsilon}_{n+1}$ at the converged configuration. We note that

$$\frac{\partial \mathbf{x}}{\partial \boldsymbol{\epsilon}_{n+1}} = \begin{bmatrix} \frac{\partial \Delta \lambda_m}{\partial \boldsymbol{\epsilon}_{n+1}} \\ \frac{\partial \boldsymbol{\epsilon}_{m,n+1}^p}{\partial \boldsymbol{\epsilon}_{n+1}} \\ \frac{\partial \Delta \lambda_w}{\partial \boldsymbol{\epsilon}_{n+1}} \\ \frac{\partial \boldsymbol{\epsilon}_{w,n+1}^p}{\partial \boldsymbol{\epsilon}_{n+1}} \end{bmatrix}_{14 \times 6}, \quad (58)$$

and thus, we can evaluate $\partial \boldsymbol{\epsilon}_{m,n+1}^p / \partial \boldsymbol{\epsilon}_{n+1}$ and $\partial \boldsymbol{\epsilon}_{w,n+1}^p / \partial \boldsymbol{\epsilon}_{n+1}$.

The partial derivatives appearing in Eqs. (47) and (57) are elaborated further in Appendix A.

(b) *Semi-plastic loading process on f_m :*

For the semi-plastic loading process on f_m , only the yield surface f_m is active, and the plastic strain for f_w remains unchanged, i.e., $\boldsymbol{\epsilon}_{w,n+1}^p = \boldsymbol{\epsilon}_{w,n}^p$ and $\Delta \lambda_w = 0$. The return mapping algorithm reduces to that for the anisotropic modified Cam-Clay model reported in [74, 108]. For this case, we just need to solve the discrete consistency condition and incremental flow rule for f_m (Eqs. (45a) and (46a)) for $\boldsymbol{\epsilon}_{m,n+1}^p$ and $\Delta \lambda_m$.

The residual vector and the unknown vector reduces to

$$\mathcal{R} = [\mathcal{R}_1 \quad \mathcal{R}_2]^\top, \quad (59)$$

and

$$\mathbf{x} = [\Delta \lambda_m \quad \boldsymbol{\epsilon}_{m,n+1}^p]^\top. \quad (60)$$

The linearized system for the Newton-Raphson scheme then takes the form

$$\begin{bmatrix} \mathcal{J}_{11} & \mathcal{J}_{12} \\ \mathcal{J}_{21} & \mathcal{J}_{22} \end{bmatrix} \begin{bmatrix} \delta \Delta \lambda_m \\ \delta \boldsymbol{\epsilon}_{m,n+1}^p \end{bmatrix} = - \begin{bmatrix} \mathcal{R}_1 \\ \mathcal{R}_2 \end{bmatrix}, \quad (61)$$

For the semi-plastic process on f_m , the Jacobian matrix \mathcal{J} becomes a 7×7 matrix. To calculate the algorithmic tangent operator \mathbb{C} , we follow the same step for the fully plastic process shown in Eqs. (53–58), which yields

$$\mathbb{C} = \mathbb{C}^e : \left(\mathbb{I} - \frac{\partial \boldsymbol{\epsilon}_{m,n+1}^p}{\partial \boldsymbol{\epsilon}_{n+1}} \right). \quad (62)$$

We solve Eq. (56) again for $\partial \mathbf{x} / \partial \boldsymbol{\epsilon}_{n+1}$ with

$$\frac{\partial \mathcal{R}}{\partial \Delta \boldsymbol{\epsilon}} \Big|_x = \begin{bmatrix} \frac{\partial f_m}{\partial \boldsymbol{\sigma}} : \mathbb{C}^e \\ \Delta \lambda_m \frac{\partial^2 f_m}{\partial \boldsymbol{\sigma}^2} : \mathbb{C}^e \end{bmatrix}_{7 \times 6}. \quad (63)$$

Thus, we can evaluate $\partial \boldsymbol{\epsilon}_{m,n+1}^p / \partial \boldsymbol{\epsilon}_{n+1}$ from the submatrix of the expression

$$\frac{\partial \mathbf{x}}{\partial \boldsymbol{\epsilon}_{n+1}} = \begin{bmatrix} \frac{\partial \Delta \lambda_m}{\partial \boldsymbol{\epsilon}_{n+1}} \\ \frac{\partial \boldsymbol{\epsilon}_{m,n+1}^p}{\partial \boldsymbol{\epsilon}_{n+1}} \end{bmatrix}_{7 \times 6}. \quad (64)$$

(c) *Semi-plastic loading process on f_w :*

The only difference here is that f_w is the active yield surface. Plastic strain for f_m remains unchanged, and $\boldsymbol{\epsilon}_{m,n+1}^p = \boldsymbol{\epsilon}_{m,n}^p$, $p_{c,n+1} = p_{c,n}$, and $\Delta \lambda_m = 0$. For the return mapping algorithm, we only need to solve the discrete consistency condition and incremental flow rule for f_w (Eqs. (45b) and (46b)) for $\boldsymbol{\epsilon}_{w,n+1}^p$ and $\Delta \lambda_w$.

The residual vector and the unknown vector now reduce to

$$\mathcal{R} = [\mathcal{R}_3 \quad \mathcal{R}_4]^\top, \quad (65)$$

and

$$\mathbf{x} = [\Delta \lambda_w \quad \boldsymbol{\epsilon}_{w,n+1}^p]^\top. \quad (66)$$

The linearized system for the Newton-Raphson scheme is

$$\begin{bmatrix} \mathcal{J}_{33} & \mathcal{J}_{34} \\ \mathcal{J}_{43} & \mathcal{J}_{44} \end{bmatrix} \begin{bmatrix} \delta \Delta \lambda_w \\ \delta \boldsymbol{\epsilon}_{w,n+1}^p \end{bmatrix} = - \begin{bmatrix} \mathcal{R}_3 \\ \mathcal{R}_4 \end{bmatrix}, \quad (67)$$

while the Jacobian \mathcal{J} is now a 7×7 matrix. To calculate the algorithmic tangent operator \mathbb{C} , we again follow the same step for the fully plastic process shown in Eqs. (53–58) and obtain

$$\mathbb{C} = \mathbb{C}^e : \left(\mathbb{I} - \frac{\partial \boldsymbol{\epsilon}_{w,n+1}^p}{\partial \boldsymbol{\epsilon}_{n+1}} \right). \quad (68)$$

We solve Eq. (56) again for $\partial \mathbf{x} / \partial \boldsymbol{\epsilon}_{n+1}$ with

$$\frac{\partial \mathcal{R}}{\partial \Delta \boldsymbol{\epsilon}} \Big|_x = \begin{bmatrix} \frac{\partial f_w}{\partial \boldsymbol{\sigma}} : \mathbb{C}^e \\ \Delta \lambda_w \frac{\partial^2 g_w}{\partial \boldsymbol{\sigma}^2} : \mathbb{C}^e \end{bmatrix}_{7 \times 6}. \quad (69)$$

Again, we can evaluate $\partial \boldsymbol{\epsilon}_{w,n+1}^p / \partial \boldsymbol{\epsilon}_{n+1}$ as a submatrix in

$$\frac{\partial \mathbf{x}}{\partial \boldsymbol{\epsilon}_{n+1}} = \begin{bmatrix} \frac{\partial \Delta \lambda_w}{\partial \boldsymbol{\epsilon}_{n+1}} \\ \frac{\partial \boldsymbol{\epsilon}_{w,n+1}^p}{\partial \boldsymbol{\epsilon}_{n+1}} \end{bmatrix}_{7 \times 6}. \quad (70)$$

4 Model validation

In this section, we validate the double-yield-surface plasticity theory using triaxial compression experimental data from three different types of transversely isotropic rocks, namely NW-Spain slate [1], Longmaxi shale [93], and a

synthetic transversely isotropic rock [84]. The aim of the validation is to reproduce the experimentally observed undulatory variation of rock strength with bedding orientation observed for these rocks.

4.1 Synthetic transversely isotropic rock

Synthetic rock is an artificially simulated material that has similar properties to those of natural rocks. It is a common man-made material for physical modeling produced by mixing water and rock-like components including sand, kaolinite, cement, resin, and curing for a certain period of time. Tien et al. [84] prepared two synthetic rocks with different weight ratios of water, cement, and kaolinite to result in different strength and stiffness for the two materials. They then layered the two materials in an alternating fashion to generate a synthetic transversely isotropic rock. The joints of the layers then represent the weak bedding planes of the rock.

Zhao et al. [108] used the anisotropic modified Cam-Clay model described in this paper to model plastic deformation in the solid matrix and reproduce the variation of rock strength with bedding orientation for the synthetic transversely isotropic rock measured in triaxial compression under a confining pressure of 14 MPa. Their result is shown by the dashed curve in Fig. 5 and reveals some deviation of an experimental data point at bedding plane orientation of 60° . Tien et al. [84] reported that the observed failure modes in the tested rock included sliding along the weak planes. Such discrepancy highlights the need for additional modeling of the failure mechanism along the weak planes on top of the plastic deformation predicted by the anisotropic modified Cam-Clay model.

We use the proposed double-yield-surface plasticity theory to better fit the experimental data of Tien et al. [84]. The parameters in the model are reported in Table 1. The elastic parameters are determined through homogenization of the parameters of the two constituent materials of the

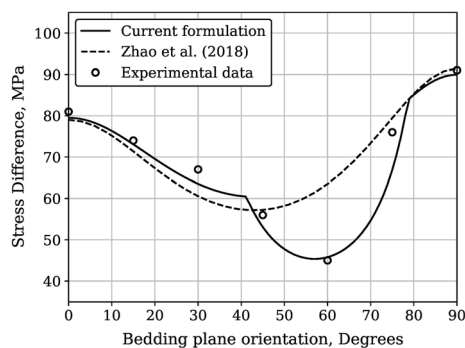


Fig. 5 Variation of rock strength with bedding orientation for synthetic transversely isotropic rocks. Experimental data are from Tien et al. [84]

Table 1 Parameters for synthetic transversely isotropic rocks

	Value	Unit
Elasticity		
λ	5335	MPa
a	-400	MPa
b	1428	MPa
μ_T	6869	MPa
μ_L	6315	MPa
Parameters for f_m		
c_1	0.82	-
c_2	-0.29	-
c_3	0.36	-
M	1.7	-
λ^p	0.0026	-
p_{c0}	-14	MPa
Parameters for f_w		
c_w	8.5	MPa
ϕ_w	24	Degrees
ψ_w	24	Degrees

synthetic transversely isotropic rocks based on Backus average [5], while the plastic parameters are calibrated to fit the experimental data. As one can see in Fig. 5, the calibrated model reproduces the undulatory variation of rock strength with bedding orientation quite well. The portion of the curve that protrudes downward is the result of the activation of yield surface f_w . Besides, we also observe two clear transition points on the curve that differentiates the failure modes through the solid matrix and along the weak planes. The range of bedding plane orientation for the sliding failure mode along the weak planes is from 41° to 79° , which perfectly matches the observed range of 45° to 75° reported by Tien et al. [84].

Lastly, we also conduct a parametric study to investigate how the parameters in the yield function f_w for sliding along the weak planes, the cohesion c_w and the friction angle ϕ_w , influence the shape of the variation curve between rock strength and bedding orientation. As reported in Fig. 6, a decrease in both ϕ_w and c_w expands the range of bedding plane orientation in which the failure mode is governed by sliding along the weak planes, as well as reduces the minimum rock strength. The difference is that decreasing ϕ_w leads to a lower bedding plane orientation that corresponds to the minimum rock strength, while c_w does not have any impact on it. This is because the minimum rock strength is achieved when the bedding plane orientation is equal to $45^\circ + \phi_w/2$. We note that this critical bedding orientation depends solely on the friction angle ϕ_w and not on the dilatancy angle ψ_w , since the weak

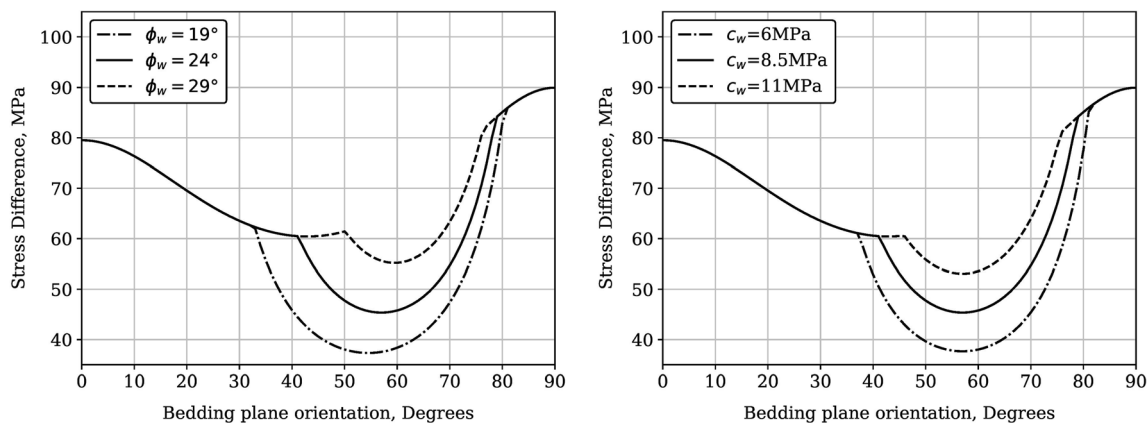


Fig. 6 Impact of mechanical parameters of the weak planes on the variation of rock strength with bedding orientation. Left: Influence of ϕ_w , Right: Influence of c_w

planes are prescribed in this case, as opposed to a continuum problem where the dilatancy angle plays a role in the inception of a shear band (see [29, 30]).

4.2 Longmaxi shale

Longmaxi shale is a black organic-rich shale from the Lower Silurian Longmaxi formation in South China. The Lower Silurian shale formation was deposited in a restricted marine basin environment and were formed under bottom water anoxic conditions [80]. In terms of the lithological composition, laminated and nonlaminated siliceous shale predominate in the Silurian Longmaxi formation [93]. To analyze the mineral composition of Longmaxi shale, Liang et al. [57] conducted X-ray diffraction analysis on 192 Longmaxi shale specimens. Their study revealed that the major components in Longmaxi shale are quartz and clay, with an average weight content of 43.2% and 39.6%, respectively. Other minor mineral components include plagioclase, potassium feldspar, calcite, dolomite, and pyrite. They also reported that the Longmaxi shale has a total organic carbon (TOC) content ranging up to 8.6%, with an average of 3.2%. The Lower Silurian Longmaxi formation has long been known as the principal source rock for conventional petroleum reservoirs [102]. In recent years, attempts have been made to exploit unconventional shale gas in this formation. Wu et al. [93] conducted triaxial compression tests on Longmaxi shale specimens extracted from the outcrops in the formation that constitutes the Chongqing Jiaoshiba shale gas block reservoirs to investigate their mechanical properties and failure modes. In this study, we will use the proposed model to reproduce the triaxial compression test response of Longmaxi shale at a confining pressure of 40 MPa.

Table 2 Parameters for Longmaxi Shale

	Value	Unit
Elasticity		
λ	52817	MPa
a	− 1416	MPa
b	23340	MPa
μ_T	16644	MPa
μ_L	9000	MPa
Parameters for f_m		
c_1	0.85	–
c_2	− 0.25	–
c_3	0.3	–
M	1.8	–
λ^p	0.0003	–
p_{c0}	− 40	MPa
Parameters for f_w		
c_w	50	MPa
ϕ_w	10	Degrees
ψ_w	10	Degrees

Wu et al. [93] reported the apparent Young's modulus and Poisson's ratio of Longmaxi shale as functions of bedding orientation in the test specimens. We used these data to calibrate the elasticity parameters for the model as shown in Table 2 and Fig. 7. In Fig. 7, we see that the calibrated model can capture the U-shaped variation of the apparent Young's modulus and the reverse U-shaped variation of Poisson's ratio with bedding orientation in the specimens. We note that there exists a 10% error between the calibrated Poisson's ratio against the measured data when the bedding orientation in the test specimen is 45°. This could be due to some adjoint plastic deformation

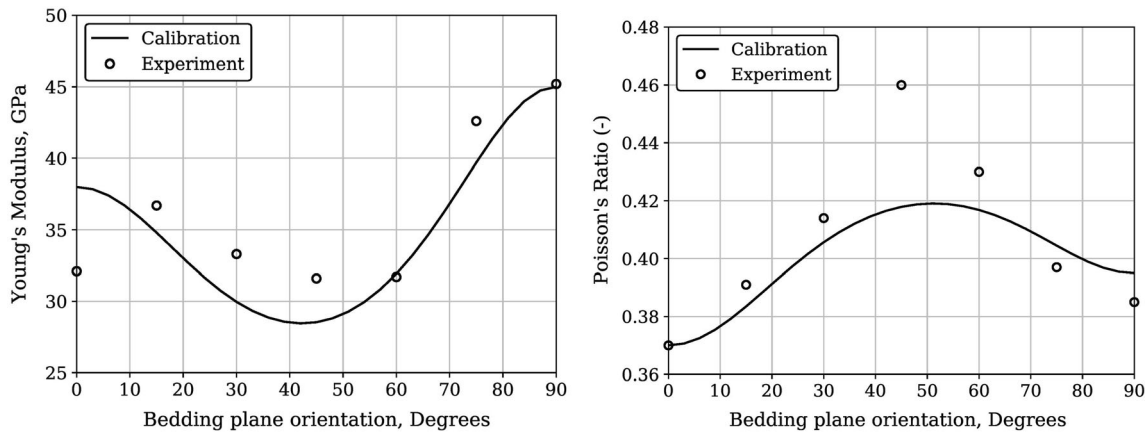


Fig. 7 Variation of elasticity parameters with bedding orientation. Left: Young’s modulus, Right: Poisson’s ratio

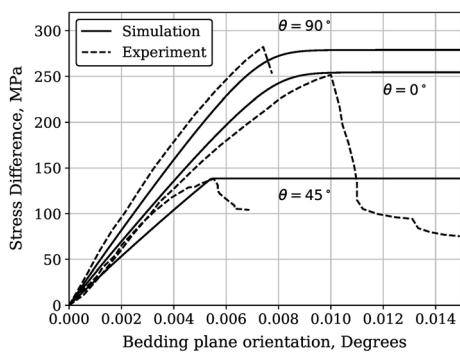


Fig. 8 Calibrated stress-strain curve for Longmaxi Shale with various bedding orientations

along the weak bedding planes that was not accounted for in the model calibration.

We next calibrate the plasticity parameters for the model shown in Table 2 by reproducing the stress-strain relationship in triaxial compression on specimens with bedding orientations of $\theta = 0, 45,$ and 90° . For $\theta = 0$ and 90° , the yield surface f_w remains inactive throughout the simulation, and the stress-strain response is governed solely by

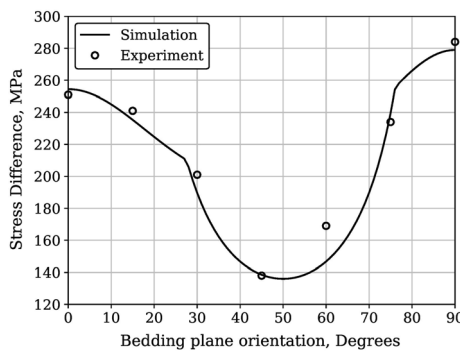


Fig. 9 Variation of rock strength with bedding orientation for Longmaxi Shale

yielding in the rock matrix. As a result, the stress gradually approaches the peak strength defined by the critical-state line of the anisotropic modified Cam-Clay model. For $\theta = 45^\circ$, the material response is initially governed by f_m , but the stress state no longer hits the critical-state line since the peak stress bounded by f_w is lower. Once the stress activates f_w , it stops changing with strain increments.

With the calibrated parameters, Fig. 9 shows the predicted variation of rock strength with bedding orientation for Longmaxi shale. It is evident that the simulation result fits the experimental data well. In addition, the model predicts that the failure mode is sliding along the weak planes for specimens with bedding orientations ranging

Table 3 Parameters for NW-Spain slate

	Value	Unit
Elasticity		
λ	83216	MPa
a	-8198	MPa
b	3947	MPa
μ_T	30447	MPa
μ_L	19520	MPa
Parameters for f_m		
c_1	0.82	-
c_2	-0.45	-
c_3	0.36	-
M	2	-
λ^p	0.001	-
p_{c0}	-10	MPa
Parameters for f_w :		
c_w	10.8	MPa
ϕ_w	17.8	Degrees
ψ_w	8.9	Degrees

from 27 to 76°. Incidentally, the failure modes reported by Wu et al. [93] indicate that specimens with $\theta = 45, 60,$ and 75° orientations tended to break down along the weak planes, in agreement with the model prediction. For $\theta = 30^\circ$, however, the specimen fractured along the diagonal direction across the rock matrix. The deviation in failure modes between the experimental observation and model prediction may be due to end constraints on the specimen. Besides, the orientation $\theta = 30^\circ$ is also near the lower limit of the predicted range, so small perturbations in the experiment may lead to an opposite result.

4.3 NW-Spain slate

In this last example, we use the proposed model to reproduce the variation of rock strength with bedding orientation for a NW-Spain slate reported by Alejano et al. [1]. The rock specimens were acquired from a quarry site located in O Barco de Valdeorras in the northwest of Spain. The slate has a black to very dark blue color and exhibits a high fissility. It possesses significant foliation patterns and is easy to fracture along the weak planes, layers of which were quarried to produce roofing slate tiles. Alejano et al. [1] conducted a series of triaxial compression tests and wave velocity tests on this slate, and showed that its mechanical behavior and failure modes are heavily dependent on the orientation of the bedding structures.

We now conduct numerical simulations of triaxial compression tests on NW-Spain slate at a confining pressure of 10 MPa. The calibrated model parameters are shown in Table 3. Here, the elasticity parameters were converted from those reported by Alejano et al. [1] measured from wave velocity tests, while the plasticity parameters were calibrated from the experimental variation of rock strength with bedding orientation in triaxial compression. As shown in Fig. 10, the model prediction fits the experimental data quite well, and also indicates that the threshold for failure along the weak planes ranges from 27

to 84°. This range matches the experimental observations where specimens with bedding orientations of 30, 45, 60, and 75° followed such a failure mode.

Alejano et al. [1] also proposed several models to capture the relationship between rock strength and bedding plane orientation for the NW-Spain slate. Their prediction with the best performance is also shown in Fig. 10. Their model consisted of two failure criteria, one for the solid matrix and the other for the weak bedding planes. For the weak planes, their failure criterion was the same as the one used in our model. Since we used the same parameter ϕ_w and c_w for the weak planes, there is an overlap of predictions with our model for cases where the failure of the slate is along the weak planes. For the rock matrix, however, they assumed that the rock strength was a linear function of the bedding plane orientation. They calibrated the model with Hoek-Brown failure criterion for specimens with bedding orientations of 0 and 90°, and interpolated the strength linearly in between. However, it has been reported by several investigators that in transversely isotropic rocks the dependence of strength with bedding orientation follows a nonlinear U-shaped variation when the sliding mechanism along the weak planes is not apparent. Thus, their linear relationship was insufficient to describe the response of the rock matrix. By comparing our prediction with that by Alejano et al. [1], it is evident that our model more realistically captures the nonlinear variation of rock strength with bedding orientation when the material fails through the rock matrix. Our model prediction also exhibits a more natural transition of the responses governed by the two failure modes.

5 Cylindrical cavity expansion in NW-Spain slate

We implement the proposed double-yield-surface plasticity model in a finite element framework built upon an open source library Deal.II [3]. We use this code to simulate the expansion of a cylindrical cavity in a transversely isotropic rock. The problem of cylindrical cavity expansion in geomaterials is widely encountered in numerous practical applications in geotechnical and petroleum engineering [21, 31, 36, 97, 101]. Applications include pressuremeter testing in shale formation [59], tunnel excavation [101], pile driving [77], and horizontal wellbore drilling [109]. Research on this topic has been extensively carried out with the surrounding geomaterials modeled by different constitutive laws. For instance, Wang et al. [91] developed an analytical solution to cylindrical cavity expansion in Mohr–Coulomb soils. Carter et al. [20] analyzed the problem with the surrounding geomaterials modeled by the Cam-Clay model. Chen and Abousleiman [22] introduced a

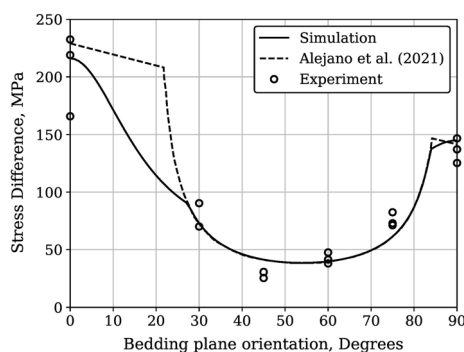


Fig. 10 Variation of rock strength with bedding orientation for NW-Spain slate

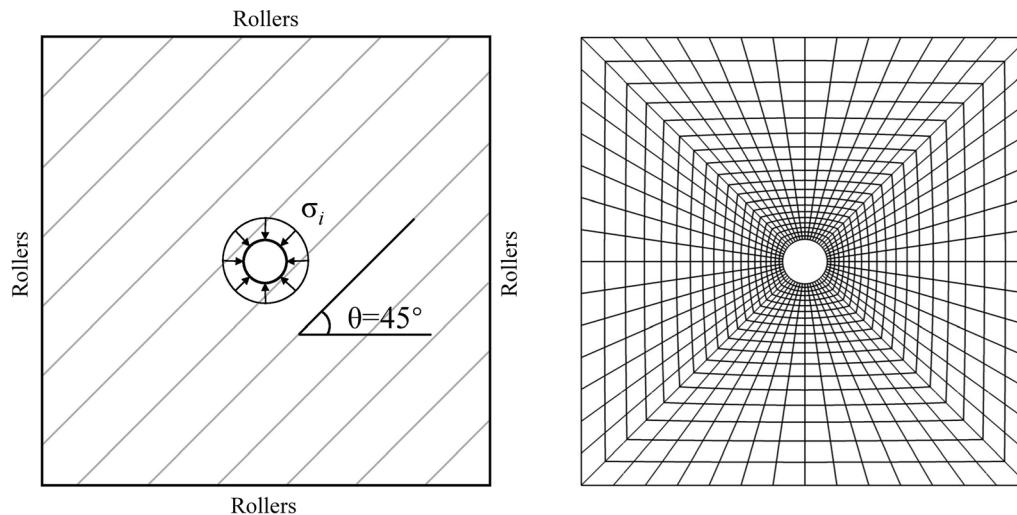


Fig. 11 Setup for the cylindrical cavity expansion problem and finite element mesh

semi-analytical method for the problem with the modified Cam-Clay soils. Li et al. [53] and Liu and Chen [58] investigated the problem considering the anisotropic mechanical properties of the surrounding soils. In this paper, we investigate the cylindrical cavity expansion problem in transversely isotropic rocks containing a borehole subjected to fluid injection.

The setup for the problem is shown on the left side of Fig. 11. The simulation domain is a $10\text{ m} \times 10\text{ m}$ square with a bedding orientation of $\theta = 45^\circ$ and deforming in plane strain. The outer boundaries of the domain are constrained with roller supports. In the middle of the domain is a cylindrical cavity of radius 0.5 m . The surrounding rock is modeled with the parameters calibrated from the NW-Spain slate, as summarized in Table 3. We assume that the surrounding rock is normally consolidated with an initial isotropic in-situ stress of p_{c0} . An injection pressure of σ_i is then prescribed on the wall of the borehole, which starts from 10 MPa and linearly increases with the loading steps to reach the target value of 100 MPa . The right side of Fig. 11 shows the finite element mesh with 1064 four-node quadrilateral elements. We conduct three sets of numerical simulations, one with the proposed double-yield-surface theory and the other two with each yield criterion f_w or f_m , and investigate the distributions of stress and plastic deformation in the surrounding rock as well as the deformed shape of the borehole.

The distributions of the mean normal stress p and deviatoric stress q are shown in Fig. 12 for the three aforementioned scenarios. The injection pressure is taken as $\sigma_i = 100\text{ MPa}$. For a clearer display, the contours were zoomed within the $6\text{ m} \times 6\text{ m}$ region in the vicinity of the borehole. Fig. 12a shows that when the surrounding rock is modeled with f_m , no significant difference in the stress field develops along the bed-parallel direction or along the bed-

normal direction. In contrast, when the surrounding rock is modeled with f_w , lower values are noted for both p and q at four corners around the borehole along the bed-parallel direction, as shown in Fig. 12b. This can attribute to the activation of the yield function f_w in these places where the stress state are bounded. Lastly, for simulations where the surrounding rocks are modeled with the double-yield-surface (DYS) plasticity model, the stress distribution in the domain is affected by both yield surfaces. The overall patterns of p and q follow those for simulation with only f_m active. At the four corners around the borehole, a lower value in the contour of q can be observed as the case with only f_w being active. Interestingly, we see that the stress components now have higher values along the bed-normal direction than along the bed-parallel direction around the borehole, compared with Fig. 12a. This is due to the plastic sliding mechanism along the bedding planes that releases the stress along the bed-parallel direction in the vicinity the borehole.

Figure 13 shows the contours of plastic strain in the simulation domain for the three aforementioned loading scenarios. We see that when only f_w is active, the plastic strain component ϵ_w^p develops and propagates from the four corners around the borehole into the surrounding rock, while for the case with the proposed double-yield-surface plasticity model, ϵ_w^p concentrates more prominently around the borehole. This is due to the fact that the stress state around the borehole is also capped by f_m , which limits the region where plastic sliding governed by f_w can occur. Comparing Fig. 13a, c, we conclude that the activation of f_w also perturbs the distribution of ϵ_m^p .

Lastly, Fig. 14 compares the deformed shapes of the borehole for the three loading scenarios. The borehole wall in the simulation with only f_w active has the least

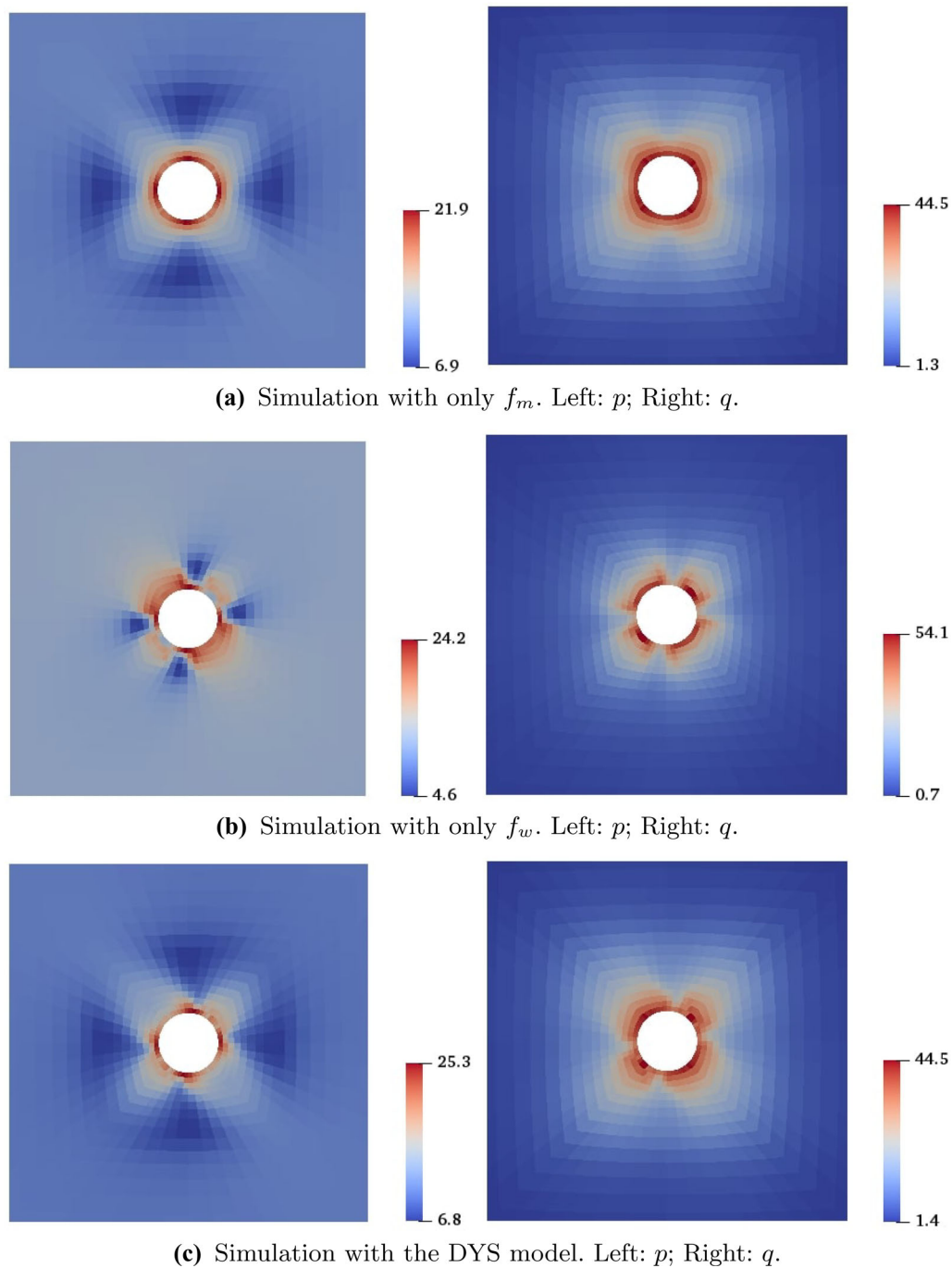


Fig. 12 Stress distribution for simulations with **a** only f_m , **b** only f_w , **c** the proposed double-yield-surface plasticity model. Left: hydrostatic component of stress, p ; Right: deviatoric component of stress, q . Color bars are stresses in MPa

deformation. In this case, the only places that undergo plastic deformation are the four corners around the borehole, while most region surrounding the borehole still deforms elastically, as shown in Fig. 13b. Deformation along the bed-normal direction of the borehole is larger than along the bed-parallel direction due to the anisotropic elastic property of the rock where the stiffness along the bed-normal direction is lower. The borehole experiences

significantly larger deformation when f_m is active. In this case, the rock surrounding the borehole undergoes volumetric plastic compaction as the material hardens to bear the injection pressure. The response predicted by the proposed double-yield-surface plasticity model is similar to that predicted when only f_m is active, but the deformation is larger at the four corners where plastic sliding mechanism occurs.

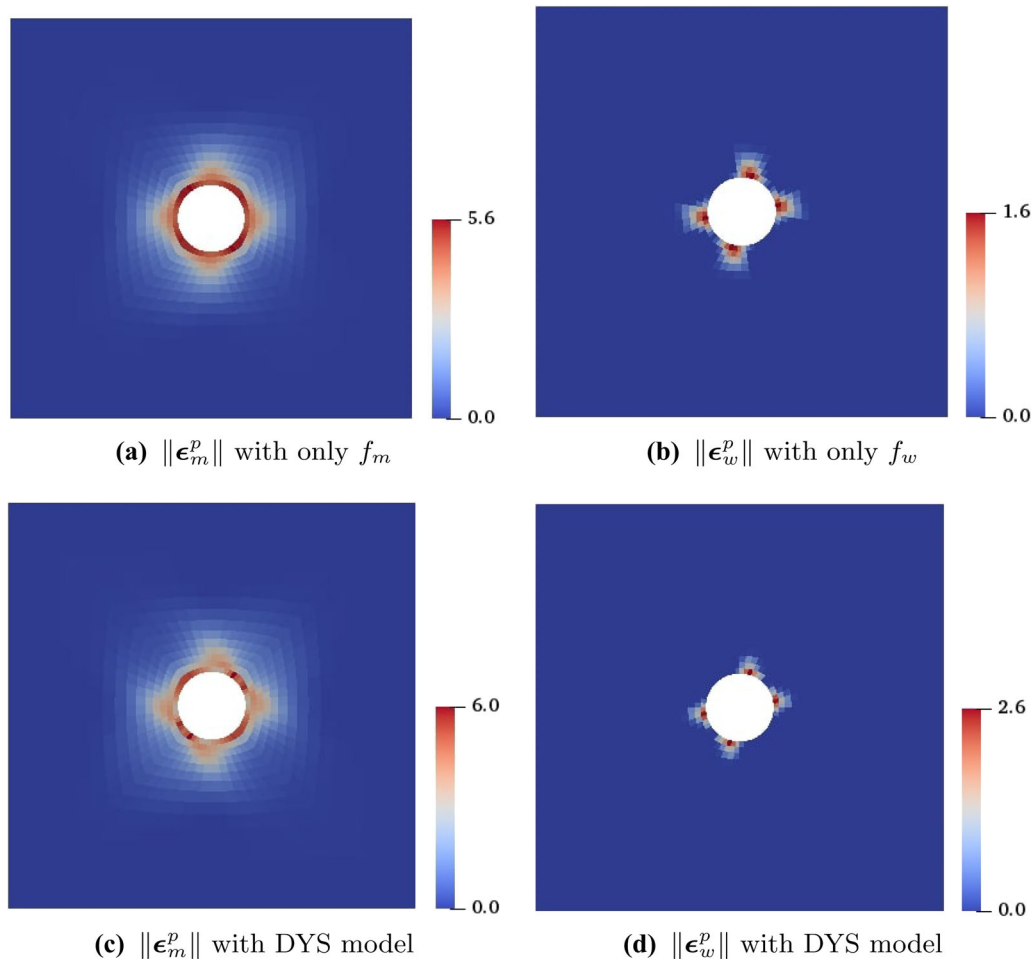


Fig. 13 Distribution of norm of plastic strain in the domain($\times 1000$). Left: Norm of plastic strain in the solid matrix $\|\epsilon_m^p\|$; Right: Norm of plastic strain along the weak bedding planes $\|\epsilon_w^p\|$

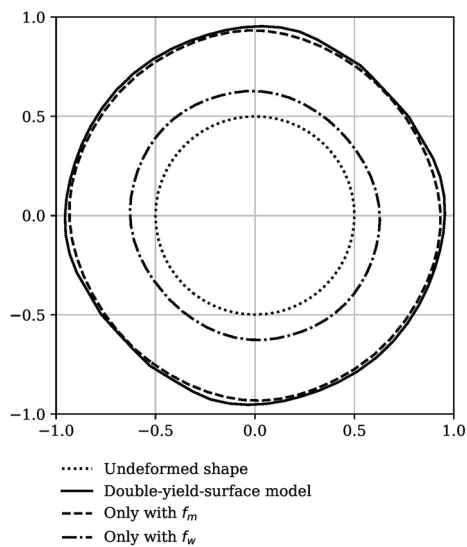


Fig. 14 Comparison of deformed shapes of the borehole. Displacement scaled by a factor of 200 for display

6 Closure

We introduced a double-yield-surface plasticity model for transversely isotropic rocks that explicitly quantifies the bulk plasticity in the rock matrix and plastic sliding along the weak planes. A recently developed anisotropic modified Cam-Clay model was used to describe the plastic response of the rock matrix, while the Mohr–Coulomb friction law was used to represent plastic sliding along the weak planes. An implicit return mapping algorithm that systematically identifies the active yield constraint(s) was developed for the numerical implementation of the constitutive model.

We validated the proposed model with triaxial compression test data for three transversely isotropic rocks, including the NW-Spain slate, the Longmaxi shale, and a synthetic transversely isotropic rock. We showed that the proposed model can reproduce the complex undulatory variation of rock strength with bedding orientation for all three rocks. By using two distinctive mechanisms of plastic

responses in the rock, the threshold of the bedding plane orientation can be identified for the two failure modes.

We used the new model to analyze the problem of cylindrical cavity expansion in a transversely isotropic rock assuming three scenarios, one in which the elastoplastic property of the rock is described by the double-yield-surface plasticity theory and the other two in which either only bulk plasticity or plastic sliding is considered. The numerical results suggest that combining bulk plasticity and plastic sliding can result in rock responses that differ significantly from those obtained by considering the two plastic mechanisms separately.

Appendix A. Relevant partial derivatives

This Appendix derives the partial derivatives of f_w and f_m . For partial derivatives associated with f_m , we have

$$\frac{\partial f_m}{\partial \boldsymbol{\sigma}} = \frac{\mathbb{A}^* : \boldsymbol{\sigma}}{M^2} + (2\mathbf{a}^* : \boldsymbol{\sigma} - p_c)\mathbf{a}^*, \tag{71}$$

$$\frac{\partial^2 f_m}{\partial \boldsymbol{\sigma}^2} = \frac{\mathbb{A}^*}{M^2} + 2\mathbf{a}^* \otimes \mathbf{a}^*, \tag{72}$$

$$\frac{\partial f_m}{\partial p_c} = \mathbf{a}^* : \boldsymbol{\sigma}, \tag{73}$$

$$\frac{\partial p_c}{\partial \epsilon_p^v} = -\frac{p_c}{\lambda_p}. \tag{74}$$

For partial derivatives associated with f_w and g_w , we limit the discussion to 2D plane strain problem and define \mathbf{l} as the tangential direction of the weak plane. The traction vector \mathbf{t} on the weak plane is

$$\mathbf{t} = \boldsymbol{\sigma} \cdot \mathbf{n}. \tag{75}$$

We can evaluate the shear stress τ and normal stress σ_n on the weak plane as

$$\sigma_n = \mathbf{n} \cdot \mathbf{t} = \boldsymbol{\sigma} : \mathbf{m}, \tag{76a}$$

$$\tau = \mathbf{l} \cdot \mathbf{t} = \boldsymbol{\sigma} : \boldsymbol{\alpha}, \tag{76b}$$

where

$$\boldsymbol{\alpha} = \frac{1}{2}(\mathbf{l} \otimes \mathbf{n} + \mathbf{n} \otimes \mathbf{l}). \tag{77}$$

Thus,

$$\frac{\partial f_w}{\partial \boldsymbol{\sigma}} = \text{sgn}(\tau)\boldsymbol{\alpha} + \tan\phi_w \mathbf{m}, \tag{78}$$

$$\frac{\partial^2 f_w}{\partial \boldsymbol{\sigma}^2} = \mathbb{0}, \tag{79}$$

$$\frac{\partial g_w}{\partial \boldsymbol{\sigma}} = \text{sgn}(\tau)\boldsymbol{\alpha} + \tan\psi_w \mathbf{m}, \tag{80}$$

$$\frac{\partial^2 g_w}{\partial \boldsymbol{\sigma}^2} = \mathbb{0}, \tag{81}$$

where $\text{sgn}(\tau)$ is the sign of τ .

Appendix B. Jacobian matrix

The submatrices \mathcal{J}_{ij} in the Jacobian matrix \mathcal{J} for the fully plastic process are given as follows:

$$\mathcal{J}_{11} = 0, \tag{82}$$

$$\mathcal{J}_{12} = -\frac{\partial f_m}{\partial \boldsymbol{\sigma}} : \mathbb{C}^e + \mathbf{a}^* : \boldsymbol{\sigma}_{n+1} \frac{p_c}{\lambda_p} \mathbf{1}, \tag{83}$$

$$\mathcal{J}_{13} = 0, \tag{84}$$

$$\mathcal{J}_{14} = -\frac{\partial f_m}{\partial \boldsymbol{\sigma}} : \mathbb{C}^e, \tag{85}$$

$$\mathcal{J}_{21} = \frac{\partial f_m}{\partial \boldsymbol{\sigma}}, \tag{86}$$

$$\mathcal{J}_{22} = -\mathbb{1} - \Delta\lambda_m \left[\left(\frac{\mathbb{A}^*}{M^2} + 2\mathbf{a}^* \otimes \mathbf{a}^* \right) : \mathbb{C}^e - \frac{p_{c,n+1}}{\lambda_p} \mathbf{a}^* \otimes \mathbf{1} \right], \tag{87}$$

$$\mathcal{J}_{23} = \mathbf{0}, \tag{88}$$

$$\mathcal{J}_{24} = -\Delta\lambda_m \left(\frac{\mathbb{A}^*}{M^2} + 2\mathbf{a}^* \otimes \mathbf{a}^* \right) : \mathbb{C}^e, \tag{89}$$

$$\mathcal{J}_{31} = 0, \tag{90}$$

$$\mathcal{J}_{32} = -\frac{\partial f_w}{\partial \boldsymbol{\sigma}} : \mathbb{C}^e, \tag{91}$$

$$\mathcal{J}_{33} = 0, \tag{92}$$

$$\mathcal{J}_{34} = -\frac{\partial f_w}{\partial \boldsymbol{\sigma}} : \mathbb{C}^e, \tag{93}$$

$$\mathcal{J}_{41} = \mathbf{0}, \tag{94}$$

$$\mathcal{J}_{42} = \mathbb{0}, \tag{95}$$

$$\mathcal{J}_{43} = \frac{\partial g_w}{\partial \boldsymbol{\sigma}}, \tag{96}$$

$$\mathcal{J}_{44} = -\mathbb{1}. \tag{97}$$

The expressions above are given in tensorial expression for brevity, but they should be converted to matrix form for numerical implementation. Rank-two and rank-four tensors transform to 1×6 vectors and 6×6 matrices in 3D, respectively.

Acknowledgements This material is based upon work supported by the U.S. Department of Energy, Office of Science, Office of Basic Energy Sciences, Geosciences Research Program, under Award Number DE-FG02-03ER15454, and by the National Science Foundation, USA, under Award Number CMMI-1914780. The first author also acknowledges the support from the Shuimu Scholar Program at Tsinghua University.

Data availability statement The datasets generated during the course of this study are available from the corresponding author upon reasonable request.

References

- Alejano LR, González-Fernández MA, Estévez-Ventosa X, Song F, Delgado-Martín J, Muñoz-Ibáñez A, González-Molano N, Alvarellos J (2021) Anisotropic deformability and strength of slate from NW-Spain. *Int J Rock Mech Min Sci* 148:104923
- Aliabadian Z, Zhao GF, Russell AR (2019) Failure, crack initiation and the tensile strength of transversely isotropic rock using the Brazilian test. *Int J Rock Mech Min Sci* 122:104073
- Arndt D, Bangerth W, Blais B, Fehling M, Gasmöller R, Heister T, Heltai L, Köcher U, Kronbichler M, Maier M (2021) The deal. II library, version 9.3. *J Numer Math* 29(3):171–186
- Asaro RJ (1983) Micromechanics of crystals and polycrystals. *Adv Appl Mech* 23:1–115
- Backus GE (1962) Long-wave elastic anisotropy produced by horizontal layering. *J Geophys Res* 67(11):4427–4440
- Bažant ZP, Oh BH (1985) Microplane model for progressive fracture of concrete and rock. *J Eng Mech* 111(4):559–582
- Bažant ZP, Ožbolt J (1990) Nonlocal microplane model for fracture, damage, and size effect in structures. *J Eng Mech* 116(11):2485–2505
- Bažant ZP, Prat PC (1988) Microplane model for brittle-plastic material: I. Theory. *J Eng Mech* 114(10):1672–1688
- Bennett KC, Regueiro RA, Luscher DJ (2019) Anisotropic finite hyper-elastoplasticity of geomaterials with Drucker–Prager/Cap type constitutive model formulation. *Int J Plast* 123:224–250
- Bennett KC, Berla LA, Nix WD, Borja RI (2015) Instrumented nanoindentation and 3D mechanistic modeling of a shale at multiple scales. *Acta Geotech* 10:1–14
- Boehler JP, Sawczuk A (1977) On yielding of oriented solids. *Acta Mech* 27(1):185–204
- Borja RI, Hsieh HS, Kavazanjian JE (1990) Double-yield-surface model. II: Implementation and verification. *J Geotech Eng* 116(9):1402–1421
- Borja RI, Wren JR (1993) Discrete micromechanics of elastoplastic crystals. *Int J Numer Meth Eng* 36(22):3815–3840
- Borja RI (2013) *Plasticity modeling & computation*. Springer, Berlin
- Borja RI, Rahmani H (2012) Computational aspects of elastoplastic deformation in polycrystalline solids. *J Appl Mech* 79(3):031024
- Borja RI, Rahmani H (2014) Discrete micromechanics of elastoplastic crystals in the finite deformation range. *Comput Methods Appl Mech Eng* 275:234–263
- Borja RI, Yin Q, Zhao Y (2020) Cam-Clay plasticity. Part IX: on the anisotropy, heterogeneity, and viscoplasticity of shale. *Comput Methods Appl Mech Eng* 360:112695
- Bryant EC, Sun W (2019) A micromorphically regularized Cam-clay model for capturing size-dependent anisotropy of geomaterials. *Comput Methods Appl Mech Eng* 354:56–95
- Cao RH, Yao R, Hu T, Wang C, Li K, Meng J (2021) Failure and mechanical behavior of transversely isotropic rock under compression-shear tests: laboratory testing and numerical simulation. *Eng Fract Mech* 241:107389
- Carter JP, Randolph MF, Wroth CP (1979) Stress and pore pressure changes in clay during and after the expansion of a cylindrical cavity. *Int J Numer Anal Meth Geomech* 3(4):305–322
- Chang M, Teh CI, Cao LF (2001) Undrained cavity expansion in modified Cam clay II: application to the interpretation of the piezocone test. *Géotechnique* 51(4):335–350
- Chen SL, Abousleiman YN (2012) Exact undrained elastoplastic solution for cylindrical cavity expansion in modified Cam Clay soil. *Géotechnique* 62(5):447–456
- Choo J, Semnani SJ, White JA (2021) An anisotropic viscoplasticity model for shale based on layered microstructure homogenization. *Int J Numer Anal Meth Geomech* 45(4):502–520
- Crook AJ, Yu JG, Willson SM (2002). Development of an orthotropic 3D elastoplastic material model for shale. In SPE/ISRM rock mechanics conference. OnePetro
- Cudny M, Staszewska K (2021) A hyperelastic model for soils with stress-induced and inherent anisotropy. *Acta Geotechnica* 16:1–19
- Cusatis G, Beghini A, Bažant ZP (2008) Spectral stiffness microplane model for quasibrittle composite laminates–Part I: theory. *J Appl Mech* 75(2):021009
- Dambly MLT, Nejati M, Vogler D, Saar MO (2019) On the direct measurement of shear moduli in transversely isotropic rocks using the uniaxial compression test. *Int J Rock Mech Min Sci* 113:220–240
- Dejaloud H, Rezaia M (2021) Adaptive anisotropic constitutive modeling of natural clays. *Int J Numer Anal Methods Geomech* 25:1756–1790
- del Castillo EM, Fávero Neto AH, Borja RI (2021) Fault propagation and surface rupture in geologic materials with a meshfree continuum method. *Acta Geotech* 16:2463–2486
- del Castillo EM, Fávero Neto AH, Borja RI (2021) A continuum meshfree method for sandbox-style numerical modeling of accretionary and doubly vergent wedges. *J Struct Geol* 153:104466
- Dong Y, Fatahi B, Khabbaz H (2020) Three dimensional discrete element simulation of cylindrical cavity expansion from zero initial radius in sand. *Comput Geotech* 117:103230
- Faizi SA, Kwok CY, Duan K (2020) The effects of intermediate principle stress on the mechanical behavior of transversely isotropic rocks: insights from DEM simulations. *Int J Numer Anal Meth Geomech* 44(9):1262–1280
- Gholami R, Rasouli V (2014) Mechanical and elastic properties of transversely isotropic slate. *Rock Mech Rock Eng* 47(5):1763–1773
- Gol'denblat II, Kopnov VA (1965) Strength of glass-reinforced plastics in the complex stress state. *Polym Mech* 1(2):54–59
- Gong F, Di B, Wei J, Ding P, Tian H, Han J (2019) A study of the anisotropic static and dynamic elastic properties of transversely isotropic rocks. *Geophysics* 84(6):C281–C293
- Gong W, Li J, Li L, Zhang S (2017) Evolution of mechanical properties of soils subsequent to a pile jacked in natural saturated clays. *Ocean Eng* 136:209–217
- Halakatevakis N, Sofianos AI (2010) Strength of a blocky rock mass based on an extended plane of weakness theory. *Int J Rock Mech Min Sci* 47(4):568–582
- Hashagen F, De Borst R (2001) Enhancement of the Hoffman yield criterion with an anisotropic hardening model. *Comput Struct* 79(6):637–651
- Havner KS (1982) The theory of finite plastic deformation of crystalline solids. In *Mechanics of solids*. Pergamon, pp 265–302

40. Hill R (1948) A theory of the yielding and plastic flow of anisotropic metals. *Proc R Soc Lond A* 193(1033):281–297
41. Hoek E (1983) Strength of jointed rock masses. *Géotechnique* 33(3):187–223
42. Hoek E, Brown ET (1980) Empirical strength criterion for rock masses. *J Geotech Eng Div* 106(9):1013–1035
43. Hsieh HS, Kavazanjian JE, Borja RI (1990) Double-yield-surface Cam-clay plasticity model. I: theory. *J Geotech Eng* 116(9):1381–1401
44. Ip SC, Borja RI (2022) Evolution of anisotropy with saturation and its implications for the elastoplastic responses of clay rocks. *Int J Numer Anal Meth Geomech* 46(1):23–46
45. Ip SC, Choo J, Borja RI (2021) Impacts of saturation-dependent anisotropy on the shrinkage behavior of clay rocks. *Acta Geotech* 16(11):3381–3400
46. Jaeger JC (1960) Shear failure of anisotropic rocks. *Geol Mag* 97(1):65–72
47. Jerman J, Mašin D (2020) Hypoplastic and viscohypoplastic models for soft clays with strength anisotropy. *Int J Numer Anal Meth Geomech* 44(10):1396–1416
48. Kalidindi SR (1998) Incorporation of deformation twinning in crystal plasticity models. *J Mech Phys Solids* 46(2):267–290
49. Koiter WT (1960) General theorems for elastic plastic solids. *Progress Solid Mech* 1:167–221
50. Levin VM, Markov MG (2005) Elastic properties of inhomogeneous transversely isotropic rocks. *Int J Solids Struct* 42(2):393–408
51. Li C, Bažant ZP, Xie H, Rahimi-Aghdam S (2019) Anisotropic microplane constitutive model for coupling creep and damage in layered geomaterials such as gas or oil shale. *Int J Rock Mech Min Sci* 124:104074
52. Li C, Caner FC, Chau VT, Bažant ZP (2017) Spherocylindrical microplane constitutive model for shale and other anisotropic rocks. *J Mech Phys Solids* 103:155–178
53. Li J, Gong W, Li L, Liu F (2017) Drained elastoplastic solution for cylindrical cavity expansion in K 0-consolidated anisotropic soil. *J Eng Mech* 143(11):04017133
54. Li K, Cheng Y, Yin ZY, Han D, Meng J (2020) Size effects in a transversely isotropic rock under Brazilian tests: laboratory testing. *Rock Mech Rock Eng* 53:1–20
55. Li K, Yin ZY, Cheng Y, Cao P, Meng J (2020) Three-dimensional discrete element simulation of indirect tensile behaviour of a transversely isotropic rock. *Int J Numer Anal Meth Geomech* 44(13):1812–1832
56. Li K, Yin ZY, Han D, Fan X, Cao R, Lin H (2021) Size effect and anisotropy in a transversely isotropic rock under compressive conditions. *Rock Mech Rock Eng* 54(9):4639–4662
57. Liang C, Jiang Z, Zhang C, Guo L, Yang Y, Li J (2014) The shale characteristics and shale gas exploration prospects of the Lower Silurian Longmaxi shale, Sichuan Basin, South China. *J Nat Gas Sci Eng* 21:636–648
58. Liu K, Chen SL (2019) Analysis of cylindrical cavity expansion in anisotropic critical state soils under drained conditions. *Can Geotech J* 56(5):675–686
59. Liu L, Chalaturnyk R, Deisman N, Zambrano-Narvaez G (2021) Anisotropic borehole response from pressuremeter testing in deep clay shale formations. *Can Geotech J* 58(8):1159–1179
60. Liu X, Zhang X, Kong L, An R, Xu G (2021) Effect of inherent anisotropy on the strength of natural granite residual soil under generalized stress paths. *Acta Geotech* 16(12):3793–3812
61. Lü X, Zeng S, Zhao Y, Huang M, Ma S, Zhang Z (2020) Physical model tests and discrete element simulation of shield tunnel face stability in anisotropic granular media. *Acta Geotech* 15(10):3017–3026
62. Ma T, Chen P, Zhang Q, Zhao J (2016) A novel collapse pressure model with mechanical-chemical coupling in shale gas formations with multi-weakness planes. *J Nat Gas Sci Eng* 36:1151–1177
63. Na S, Sun W (2018) Computational thermomechanics of crystalline rock, Part I: a combined multi-phase-field/crystal plasticity approach for single crystal simulations. *Comput Methods Appl Mech Eng* 338:657–691
64. Niandou H, Shao JF, Henry JP, Fourmaintraux D (1997) Laboratory investigation of the mechanical behaviour of Tourne-mire shale. *Int J Rock Mech Min Sci* 34(1):3–16
65. Nova R (1986) An extended Cam Clay model for soft anisotropic rocks. *Comput Geotech* 2(2):69–88
66. Pande GN, Sharma KG (1983) Multi-laminate model of clays—a numerical evaluation of the influence of rotation of the principal stress axes. *Int J Numer Anal Meth Geomech* 7(4):397–418
67. Park B, Min KB, Thompson N, Horsrud P (2018) Three-dimensional bonded-particle discrete element modeling of mechanical behavior of transversely isotropic rock. *Int J Rock Mech Min Sci* 110:120–132
68. Pouragha M, Wan R, Eghbalian M (2019) Critical plane analysis for interpreting experimental results on anisotropic rocks. *Acta Geotech* 14(4):1215–1225
69. Przecherski P, Pietruszczak S (2020) On specification of conditions at failure in interbedded sedimentary rock mass. *Acta Geotech* 15(2):365–374
70. Ramamurthy T (1993) Strength and modulus responses of anisotropic rocks. *Compr Rock Eng* 1(13):313–329
71. Schröder J, Miehe C (1997) Aspects of computational rate-independent crystal plasticity. *Comput Mater Sci* 9(1–2):168–176
72. Semnani SJ, White JA (2020) An inelastic homogenization framework for layered materials with planes of weakness. *Comput Methods Appl Mech Eng* 370:113221
73. Semnani SJ, Borja RI (2017) Quantifying the heterogeneity of shale through statistical combination of imaging across scales. *Acta Geotech* 12:1193–1205
74. Semnani SJ, White JA, Borja RI (2016) Thermoplasticity and strain localization in transversely isotropic materials based on anisotropic critical state plasticity. *Int J Numer Anal Meth Geomech* 40(18):2423–2449
75. Shang J, Duan K, Gui Y, Handley K, Zhao Z (2018) Numerical investigation of the direct tensile behaviour of laminated and transversely isotropic rocks containing incipient bedding planes with different strengths. *Comput Geotech* 104:373–388
76. Simo JC, Kennedy JG, Govindjee S (1988) Non-smooth multi-surface plasticity and viscoplasticity. Loading/unloading conditions and numerical algorithms. *Int J Numer Meth Eng* 26(10):2161–2185
77. Singh S, Patra NR (2020) Axial behavior of tapered piles using cavity expansion theory. *Acta Geotech* 15(6):1619–1636
78. Sitarenios P, Kavvadas M (2020) A plasticity constitutive model for unsaturated, anisotropic, nonexpansive soils. *Int J Numer Anal Meth Geomech* 44(4):435–454
79. Spencer AJM (1984) Continuum theory of the mechanics of fibre-reinforced composites. Springer, New York, pp 1–32
80. Tan J, Weniger P, Krooss B, Merkel A, Horsfield B, Zhang J, Boreham CJ, van Graas G, Tocher BA (2014) Shale gas potential of the major marine shale formations in the Upper Yangtze Platform, South China, Part II: methane sorption capacity. *Fuel* 129:204–218
81. Tan X, Konietzky H, Frühwirth T, Dan DQ (2015) Brazilian tests on transversely isotropic rocks: laboratory testing and numerical simulations. *Rock Mech Rock Eng* 48(4):1341–1351
82. Tang H, Wei W, Song X, Liu F (2021) An anisotropic elastoplastic Cosserat continuum model for shear failure in stratified geomaterials. *Eng Geol* 293:106304
83. Tien YM, Kuo MC (2001) A failure criterion for transversely isotropic rocks. *Int J Rock Mech Min Sci* 38(3):399–412

84. Tien YM, Kuo MC, Juang CH (2006) An experimental investigation of the failure mechanism of simulated transversely isotropic rocks. *Int J Rock Mech Min Sci* 43(8):1163–1181
85. Togashi Y, Kikumoto M, Tani K (2017) An experimental method to determine the elastic properties of transversely isotropic rocks by a single triaxial test. *Rock Mech Rock Eng* 50(1):1–15
86. Tsai SW, Wu EM (1971) A general theory of strength for anisotropic materials. *J Compos Mater* 5(1):58–80
87. Ueda K, Iai S (2019) Constitutive modeling of inherent anisotropy in a strain space multiple mechanism model for granular materials. *Int J Numer Anal Meth Geomech* 43(3):708–737
88. Ueda K, Iai S (2021) Noncoaxiality considering inherent anisotropy under various loading paths in a strain space multiple mechanism model for granular materials. *Int J Numer Anal Meth Geomech* 45(6):815–842
89. Walsh J, Brace WF (1964) A fracture criterion for brittle anisotropic rock. *J Geophys Res* 69(16):3449–3456
90. Wang TT, Huang TH (2009) A constitutive model for the deformation of a rock mass containing sets of ubiquitous joints. *Int J Rock Mech Min Sci* 46(3):521–530
91. Wang Y, Chen H, Li J, Sun DA (2021) Analytical solution to cylindrical cavity expansion in Mohr–Coulomb soils subject to biaxial stress condition. *Int J Geomech* 21(9):04021152
92. Wang Z, Zong Z, Qiao L, Li W (2018) Elastoplastic model for transversely isotropic rocks. *Int J Geomech* 18(2):04017149
93. Wu Y, Li X, He J, Zheng B (2016) Mechanical properties of longmaxi black organic-rich shale samples from south china under uniaxial and triaxial compression states. *Energies* 9(12):1088
94. Xu G, Gutierrez M, He C, Meng W (2020) Discrete element modeling of transversely isotropic rocks with non-continuous planar fabrics under Brazilian test. *Acta Geotechnica* 15:1–28
95. Xu G, Gutierrez M, He C, Wang S (2021) Modeling of the effects of weakness planes in rock masses on the stability of tunnels using an equivalent continuum and damage model. *Acta Geotechnica* 16:1–22
96. Xue L, Yu JK, Pan JH, Wang R, Zhang JM (2021) Three-dimensional anisotropic plasticity model for sand subjected to principal stress value change and axes rotation. *Int J Numer Anal Meth Geomech* 45(3):353–381
97. Yang C, Gong W, Li J, Gu X (2020) Drained cylindrical cavity expansion in modified Cam-clay soil under biaxial in-situ stresses. *Comput Geotech* 121:103494
98. Yang SQ, Yin PF, Li B, Yang DS (2020) Behavior of transversely isotropic shale observed in triaxial tests and Brazilian disc tests. *Int J Rock Mech Min Sci* 133:104435
99. Yin PF, Yang SQ, Tian WL, Cheng JL (2019) Discrete element simulation on failure mechanical behavior of transversely isotropic rocks under different confining pressures. *Arab J Geosci* 12(19):1–21
100. Yin Q, Liu Y, Borja RI (2021) Mechanisms of creep in shale from nanoscale to specimen scale. *Comput Geotech* 136:104138
101. Yu HS (2000) *Cavity expansion methods in geomechanics*. Springer, Berlin
102. Zhang JP, Tang SH, Guo DX (2011) Shale gas favorable area prediction of the Qiongzhusi Formation and Longmaxi Formation of lower Palaeozoic in Sichuan Basin, China. *Geol Bull China* 30(2–3):357–363
103. Zhang Q, Choo J, Borja RI (2019) On the preferential flow patterns induced by transverse isotropy and non-Darcy flow in double porosity media. *Comput Methods Appl Mech Eng* 353:570–592
104. Zhang Q, Borja RI (2021) Poroelastic coefficients for anisotropic single and double porosity media. *Acta Geotechnica* 16:1–13
105. Zhao Y, Borja RI (2019) Deformation and strength of transversely isotropic rocks. In: *Desiderata Geotechnica*. Springer, Cham, pp 237–241
106. Zhao Y, Borja RI (2020) A continuum framework for coupled solid deformation-fluid flow through anisotropic elastoplastic porous media. *Comput Methods Appl Mech Eng* 369:113225
107. Zhao Y, Borja RI (2021) Anisotropic elastoplastic response of double-porosity media. *Comput Methods Appl Mech Eng* 380:113797
108. Zhao Y, Semnani SJ, Yin Q, Borja RI (2018) On the strength of transversely isotropic rocks. *Int J Numer Anal Meth Geomech* 42(16):1917–1934
109. Zhou H, Liu H, Kong G, Huang X (2014) Analytical solution of undrained cylindrical cavity expansion in saturated soil under anisotropic initial stress. *Comput Geotech* 55:232–239
110. Zhu Y, Tsvankin I, Dewangan P, Wijk KV (2007) Physical modeling and analysis of P-wave attenuation anisotropy in transversely isotropic media. *Geophysics* 72(1):D1–D7
111. Zienkiewicz OC, Pande GN (1977) Time-dependent multilaminate model of rocks—a numerical study of deformation and failure of rock masses. *Int J Numer Anal Meth Geomech* 1(3):219–247

Publisher's Note Springer Nature remains neutral with regard to jurisdictional claims in published maps and institutional affiliations.